

**ELM Suppression and Pedestal Structure in I-Mode Plasmas on  
Alcator C-Mod**

by

John Reel Walk, Jr.

S.B. Physics & Mathematics (2010)  
Massachusetts Institute of Technology

Submitted to the Department of Nuclear Science and Engineering  
in partial fulfillment of the requirements for the degree of

Doctor of Philosophy in Applied Plasma Physics

at the

MASSACHUSETTS INSTITUTE OF TECHNOLOGY

June 2014

© Massachusetts Institute of Technology 2014. All rights reserved.

Author .....  
.....

Department of Nuclear Science and Engineering  
February 23, 2014

Certified by.....  
.....

Jerry W. Hughes  
Research Scientist, Plasma Science and Fusion Center  
Thesis Supervisor

Certified by.....  
.....

Dennis G. Whyte  
Professor, Department of Nuclear Science and Engineering  
Thesis Reader

Accepted by.....  
.....

Mujid S. Kazimi  
TEPCO Professor of Nuclear Engineering  
Chair, Department Committee on Graduate Students



**ELM Suppression and Pedestal Structure in I-Mode Plasmas on Alcator C-Mod**  
by  
John Reel Walk, Jr.

Submitted to the Department of Nuclear Science and Engineering  
on February 23, 2014, in partial fulfillment of the  
requirements for the degree of  
Doctor of Philosophy in Applied Plasma Physics

*Abstract*

Abstract goes here.

Thesis Supervisor: Jerry W. Hughes  
Research Scientist, Plasma Science and Fusion Center

Thesis Reader: Dennis G. Whyte  
Professor, Department of Nuclear Science and Engineering



A dedication goes here maybe?



## ACKNOWLEDGMENTS

---

Acknowledgements go here.



## CONTENTS

---

<b>1</b>	<b>INTRODUCTION</b>	<b>15</b>
1.1	Plasmas for Fusion	16
1.1.1	Plasma Parameters	16
1.1.2	Fusion Fuels	17
1.2	Magnetic Confinement	20
1.2.1	Basic Principles	20
1.2.2	Toroidal Configurations	23
1.3	Alcator C-Mod	27
1.4	Confinement & Transport	30
1.4.1	Global Confinement	30
1.4.2	Transport Barriers	32
1.5	Goals & Outline	34
<b>2</b>	<b>HIGH-PERFORMANCE REGIMES</b>	<b>41</b>
2.1	ELM-Free H-Mode	41
2.2	ELMy H-Mode	42
2.2.1	Global Parameters	42
2.2.2	Fluctuations and ELMs	42
2.2.3	Active ELM Control	42
2.3	ELM-Suppressed H-Modes	42
2.3.1	QH-Mode	42
2.3.2	EDA H-Mode	42
2.4	I-Mode	42
2.4.1	Access and Operation	42
2.4.2	Global Performance	42
2.4.3	Edge Fluctuations – the Weakly-Coherent Mode	42
<b>3</b>	<b>PEDESTAL MODELING AND THEORY</b>	<b>47</b>
3.1	Empirical Models	47
3.2	MHD Stability: Peeling-Ballooning Modes	47
3.2.1	Ballooning MHD	47
3.2.2	Peeling MHD	47
3.2.3	ELITE Code	47
3.3	Turbulent Modeling	47
3.4	The EPED Model	47
<b>4</b>	<b>ELMY H-MODES ON C-MOD</b>	<b>51</b>
4.1	ELMy H-Modes Access	51
4.2	ELM Cycle Synchronization	51
4.3	EPED Model Predictions	51
4.4	$I_p$ Scan	51
4.5	Pedestal Width Scalings	51

5	I-MODE PEDESTAL SCALINGS	55
5.1	Access and Experimental Setup	55
5.2	Pedestal Responses	55
5.2.1	Pedestal Response to Fueling	55
5.2.2	Pedestal Temperature	55
5.2.3	Pressure Pedestal Scalings and Performance	55
5.3	Pedestal Widths	55
5.4	Fluctuation Characterization	55
6	I-MODE PEDESTAL STABILITY MODELING	59
6.1	MHD Stability – ELITE	59
6.2	KBM and Infinite-n MHD Stability	59
6.3	Sawtooth Perturbations of Pedestal Stability	59
6.4	Other Models	59
7	CONCLUSIONS	63
A	DIAGNOSTICS	67
A.1	Thomson Scattering	67
A.1.1	Principles of Thomson Scattering	68
A.1.2	Edge Thomson Scattering on C-Mod	76
A.2	Fast Diagnostics	76
A.3	Fluctuation Diagnostics	76
B	HIGH-RESOLUTION PEDESTAL DATABASE	79

## LIST OF FIGURES

---

- Figure 1.1 Binding energy per nucleon versus atomic mass number, with notable isotopes marked. Reactions forming nuclei with higher binding energy are exothermic – thus, fusion of elements lighter than  $^{56}\text{Fe}$  or fission of elements heavier than  $^{56}\text{Fe}$  releases energy. [9] 18
- Figure 1.2 Reaction rate normalized to fuel density, expressed as the rate coefficient  $\langle\sigma v\rangle$ , for fusion fuels as a function of temperature. Notably, deuterium-tritium fusion exhibits a higher peak reaction rate, as well as reaching that peak at a lower temperature, than other fuels. 19
- Figure 1.3 Electron and ion gyro orbits in an applied magnetic field. Note that, due to the charge dependence in the Lorentz Force (eq. (1.14)), electrons and ions orbit in opposite directions relative to the magnetic field. 21
- Figure 1.4 Example geometry of a circular-cross-section tokamak plasma, describing a torus of major radius  $R_0$  and minor radius  $a$ , with poloidal coordinate  $\theta$  and toroidal coordinate  $\Phi$ . Tokamak configurations are characterized by an applied toroidal field  $B_T$  with a toroidal plasma current  $I_p$ , which in turn generates a poloidal magnetic field  $B_p$ . 23
- Figure 1.5 Schematic of a tokamak configuration, showing the plasma and magnetic coils. The applied toroidal magnetic field is generated by the toroidal field coils (shown in blue). A toroidal plasma current is generated by the center transformer, in turn generating a poloidal magnetic field (shown in green). These combine to form the helical magnetic field. The plasma shape and equilibrium is adjusted with the outer poloidal field coils (gray). 25

- Figure 1.6 Cross-section of a tokamak plasma, illustrating closed magnetic flux surfaces (light blue), the last closed flux surface (red), and surfaces with open magnetic field lines (dark blue). Definitions for plasma shaping parameters elongation  $\kappa$ , and upper and lower triangularity  $\delta_u$ ,  $\delta_l$  are shown at right. 26
- Figure 1.7 Cutaway view of the Alcator C-Mod tokamak, including cryostat and ancillary structures, illustrating the extensive support structures necessary for compact, high-field operation. 28
- Figure 1.8 Cross-section of the C-Mod vacuum vessel, cryostat and diagnostic access ports, with toroidal-field and equilibrium-field magnetic coils labeled. Also shown is the plasma position in a typical LSN shape, with strike points in the lower divertor shown.. 29
- Figure 1.9 Diffusion coefficients and plasma profiles for a “toy model” 1D diffusion equation with a general parameter  $Q(x)$  and accompanying diffusion coefficient  $D_Q(x)$ . 33
- Figure A.1 Coordinate system considered for Thomson scattering, with the incident wave of wavenumber  $\vec{k}_i$  incident on a particle at  $\vec{r}(t')$  for retarded time  $t'$ . The scattered wave  $\vec{k}_s$  is drawn to an observer at  $\vec{R}(t')$ . 68
- Figure A.2 Definitions of the angular dependences in the Thomson scattering geometry: namely, the angle  $\theta$  between the incident wave direction  $\hat{i}$  and scattering direction  $\hat{s}$ , and the polarization angle  $\phi$  of the incident electric field  $\hat{E}_i$  with respect to the projection of  $\hat{s}$  into the polarization plane. 70
- Figure A.3 Spectral functions normalized to density and laser power, evaluated at  $\theta = \phi = \pi/2$ . The spectrum spreads farther from the laser line at higher temperature, as well as blue-shifting due to relativistic effects. 75

## LIST OF TABLES

---

Table 1.1	Summary of Alcator C-Mod typical operating parameters. 27
-----------	---

Table 2.1	Typical operating parameters of tokamaks noted in this thesis, with reference to overviews. <i>Note:</i> all ITER values are projected. <a href="#">check all values here</a> 42
Table B.1	SQL database parameters used as keys – (SHOT, TA, TB) is sufficient to uniquely identify entries in the database. 79
Table B.2	SQL database parameters used as flags for time windows. 80
Table B.3	SQL database parameters for useful measured parameters. 80
Table B.4	SQL database parameters for EFIT values. 81
Table B.5	SQL database parameters for heating power, stored energy, and confinement. 82
Table B.6	SQL database parameters for high-resolution pedestal profiles. 83
Table B.7	SQL database parameters for WCM fluctuation measurements. 84



## INTRODUCTION

---

The population of the earth is projected to increase substantially over the next half-century, potentially reaching as high as 10 billion globally by 2050 [1]. At the same time, any attempt to increase the quality of life of the existing population will necessarily involve increased energy consumption per capita, with a greater fraction of the earth approaching “first-world” consumption levels [2]. As such, worldwide energy consumption will likely continue to increase in the next few decades [3, 4]

This increase in energy demand occurs in parallel with increased pressure on traditional energy sources. Fossil fuels (oil, coal, and natural gas), while reliable sources of base-load power, nevertheless face issues. Oil faces increasing cost and technical difficulty in capturing dwindling available reserves, as well as the potential for serious ecological damage from accidents (e.g., the Deepwater Horizon offshore rig accident in 2010). Coal, while more readily available (an estimated 257 billion tons of recoverable reserves in the US, lasting roughly 240 years at current consumption [4, 5]), releases particulate matter into the atmosphere, with serious consequences both to the environment and to human health, as well as the greenhouse gases tied to deleterious climate change.

Renewable energy sources have a certain “green” appeal, but each is subject to strict limitations on their implementation. Solar and wind power suffer from a large degree of variability in their output, necessitating a combination of expensive energy storage methods or (often fossil-fuel based) backup production to handle shortfalls. Hydroelectric and geothermal power are suitable for base-load power production, but are strictly restricted in their implementation by geographic concerns – bluntly, there are relatively few locations where hydro or geothermal power generation is possible, and many of these have already been developed.

*cite for this?*

Conventional – that is, fission-based – nuclear power can also supply carbon-free base-load power, with fuel reserves lasting through the next century. While nuclear power does suffer from the potential for extremely serious accidents (Fukushima, Chernobyl) it is, in general, highly safe. However, public perception of nuclear power hinges on these safety concerns, limiting the expansion of nuclear power to meet increasing demand and the safe long-term handling of existing nuclear waste, as well as, ironically, preventing the replacement of an aging reactor fleet with newer, safer designs.

*Fusion*, the nuclear process driving stellar cores, is a potentially highly attractive option for satisfying the world's growing energy needs in an efficient, environmentally-sound manner. A fusion reactor would supply base-load power using only a small amount of an effectively inexhaustible fuel (readily available for harvesting from seawater), with no greenhouse gas emissions or meaningfully radioactive waste, and the physical impossibility of a major "meltdown" accident. However, fusion remains in the experimental stage, with significant technical hurdles remaining before the development of a prototype fusion power plant. This thesis will attempt to contribute to the understanding of one of these hurdles, regarding the requirement for efficient plasma behavior in a reactor scenario *reword this!* Further reading on the development of fusion energy is available to the interested reader in several excellent references. [6, 7, 8] •

*reword last sentence...*

## 1.1 PLASMAS FOR FUSION

A *plasma* is a gas to which sufficient energy has been applied to strip some or all of the electrons off the nuclei of its constituent atoms. These ions and electrons freely interact with one another, behaving as coupled fluids. Plasmas of interest for fusion research are comprised of light elements (typically Hydrogen or Helium), and are at extremely high temperatures, in excess of 100 million Kelvin (10 – 20 keV). As these conditions are far in excess of the ionization energy for these elements, the plasma is dominated by collisions between its charged particles, rather than interactions with bound electron states.

### 1.1.1 Plasma Parameters

As the plasma is comprised of free charged particles, it responds strongly to electric and magnetic fields. In the presence of a DC electric field (externally applied, or generated by an imbalance of positive and negative charge in the plasma), the plasma will rearrange itself to screen out the field. This effect breaks down at short length scales, at which there is an insufficient number of charge carriers to rearrange and counter the field – the characteristic scale for this effect is the Debye Length, given by

$$\lambda_D = \sqrt{\frac{\epsilon_0 T}{n e^2}} \quad (1.1)$$

At size scales significantly larger than  $\lambda_D$ , this will enforce an approximately balanced electric charge in the plasma, termed "quasi-

“neutrality”. This is reflected in the number densities of electrons and multiple ion species  $j$ , each with charge  $Z_j$ , by the relation

$$n_e = \sum_j n_j Z_j \quad (1.2)$$

In a multiple-ion species plasma, we may also define an effective ion charge

$$Z_{\text{eff}} = \frac{1}{n_e} \sum_j n_j Z_j^2 \quad (1.3)$$

The electrostatic force driving this charge redistribution induces a “ringing” oscillation in the plasma, at the characteristic plasma frequency  $\omega_p$ :

$$\omega_p = \sqrt{\frac{n e^2}{\epsilon_0 m_e}} \quad (1.4)$$

This natural oscillation in the plasma also has the effect of screening AC electric fields varying at frequencies  $\omega < \omega_p$ .

Coulomb collisions between charged particles in the plasma tend to drive magnetically-confined plasmas into thermal equilibrium, with the velocity distribution for a species given by the Maxwellian

$$f(v) = n \left( \frac{m}{2\pi T} \right)^{3/2} \exp \left( -\frac{mv^2}{2T} \right) \quad (1.5)$$

These collisions also cause the plasma to emit a continuous spectrum of Bremsstrahlung radiation. For a plasma in thermal equilibrium, integration over the full spectrum gives for the total radiated power

$$P_{\text{Brems}} = (5.35 \times 10^{-37}) n_e^2 Z_{\text{eff}} \sqrt{T} \quad (1.6)$$

representing a consistent source of heat loss from the plasma.

### 1.1.2 Fusion Fuels

Fusion collectively refers to the class of nuclear reactions merging lighter nuclei into a single heavier element. While fusion reactions for elements lighter than iron are generally exothermic, as they form nuclei with greater binding energy per nucleon (see fig. 1.1), the most common and readily attainable involve isotopes of hydrogen or helium, the most promising candidates for which are shown below.



**Figure 1.1:** Binding energy per nucleon versus atomic mass number, with notable isotopes marked. Reactions forming nuclei with higher binding energy are exothermic – thus, fusion of elements lighter than  $^{56}\text{Fe}$  or fission of elements heavier than  $^{56}\text{Fe}$  releases energy. [9]



Here D and T indicate nuclei of deuterium and tritium, two heavy isotopes of hydrogen (one proton plus one and two neutrons, respectively). The fusion reaction rate  $R_f$  is given by

$$R_f = n_1 n_2 \langle \sigma v \rangle_{1,2} \quad (1.11)$$

where  $n_1$  and  $n_2$  indicate the densities of the two fuel ions (e.g., for deuterium-tritium fuel  $n_1 n_2 = n_D n_T$ , while for pure-deuterium fuel  $n_1 n_2 = \frac{1}{2} n_D^2$  to remove double-counting of fuel ions) and  $\langle \sigma v \rangle_{1,2}$  is a rate parameter incorporating the energy-dependent reaction cross-section averaged over the Maxwellian fuel distribution (eq. (1.5)). In practice, the energy-dependent cross-section is empirically determined – measured rate parameters  $\langle \sigma v \rangle$  for the fuels of interest are shown in fig. 1.2.



**Figure 1.2:** Reaction rate normalized to fuel density, expressed as the rate coefficient  $\langle\sigma v\rangle$ , for fusion fuels as a function of temperature. Notably, deuterium-tritium fusion exhibits a higher peak reaction rate, as well as reaching that peak at a lower temperature, than other fuels.

Pure deuterium fuel (reactions shown in eqs. (1.7) and (1.8)) is attractive from a research standpoint, due to the abundance and ease of use of deuterium. Deuterium is a stable nucleus, obviating the need for radiation safety in the fuel system, and is naturally occurring in relative abundance (approximately 1/6420 of hydrogen nuclei on earth are deuterium [10]), allowing harvesting of deuterium fuel from seawater. However, pure-deuterium reactions suffer from low energy output per reaction and a significantly lower reaction rate at feasible plasma conditions compared to other fuel options (see fig. 1.2), setting high performance requirements for a putative DD-burning reactor.

The D – He<sup>3</sup> reaction (eq. (1.9)) exhibits several desirable properties, namely an impressive energy yield per reaction, and the fact that the reaction produces only charged particles rather than the high-energy neutrons found in D – D and D – T reactions, which can cause significant damage to reactor materials. However, as with D – D fuel, the D – He<sup>3</sup> reaction suffers from a lower reaction rate at attainable conditions, as well as the fact that Helium-3 does not occur in economically usable quantities on Earth. While off-planet sources of Helium-3 exist (for example, a useful quantity is present in the lunar regolith [11] and in the atmospheres of some gas giants [12]), this fuel remains the subject of speculation.

The deuterium-tritium reaction (eq. (1.10)) is considered the most promising for a first-generation fusion reactor, due to its high energy output per reaction and favorable reaction cross-section – the rate parameter  $\langle\sigma v\rangle_{DT}$  reaches its peak at a lower temperature, and reaches a greater absolute level than other fusion fuels. However, D – T operation is limited both by fuel sources, and reaction products. D – T fusion produces a 14 MeV neutron, carrying roughly 80% of the energy released by the fusion reaction, which can damage unshielded reactor materials. Moreover, while deuterium is stable and readily available, tritium is radioactive with a short half-life (roughly 12.3 years), so it is not naturally occurring in meaningful quantities on earth. A reactor will solve both of these problems with a *neutron blanket*, a neutron-absorbing structure surrounding the plasma. This provides the necessary shielding for sensitive reactor components. The heat generated in the blanket from neutron absorption will also be drawn off in a steam cycle to drive turbines, generating electricity from the reactor. Finally, seeding the blanket with lithium allows the following reactions with fusion neutrons:



the Lithium-6 reaction (eq. (1.12)) absorbs “slow” neutrons (that is, neutrons that have thermalized to the blanket temperature via collisions) to produce tritium, plus additional heat. Lithium-7 (eq. (1.13)) is more likely to capture fast neutrons to produce tritium in an endothermic reaction; however, the reaction also acts as a neutron multiplier, as a free neutron is maintained through the reaction. Using blankets enriched with  ${}^6\text{Li}$ , coupled with neutron multipliers, a reactor will target an over-unity tritium breeding ratio, with  $> 1$  tritons produced per neutron entering the blanket (i. e., per tritium consumed in a fusion reaction). ●

## 1.2 MAGNETIC CONFINEMENT

### 1.2.1 Basic Principles

The temperatures in excess of 100 million Kelvin necessary for fusion in a plasma are incompatible with any contact between solid reactor materials and the hot core of the plasma. Magnetic confinement relies on the strong response of the charged particles comprising the plasma to magnetic fields, rather than a material wall, to retain the thermal pressure ( $\sim 10$  atm for a reactor) from the plasma. The response of

**Figure 1.3:** Electron and ion gyro orbits in an applied magnetic field. Note that, due to the charge dependence in the Lorentz Force (eq. (1.14)), electrons and ions orbit in opposite directions relative to the magnetic field.



a charged particle to electric and magnetic fields is governed by the Lorentz force,

$$\vec{F} = q \left( \vec{E} + \vec{v} \times \vec{B} \right) \quad (1.14)$$

In a strong background magnetic field, the particle will move on a helical path along the field line. The  $\vec{v} \times \vec{B}$  factor in the Lorentz Force causes the particle to experience no magnetic force parallel to the field, while velocity perpendicular to the field generates a force proportional to the velocity times the magnetic field, directed perpendicular to both – thus the particle freely streams parallel to the field, but is trapped in a circular orbit perpendicular to it, termed “gyro motion”, shown in fig. 1.3. The particle will orbit at the cyclotron frequency,

$$\omega_c = \frac{qB}{m} \Rightarrow \omega_{ce} = \frac{eB}{m_e}, \quad \omega_{ci} = \frac{ZeB}{m_i} \quad (1.15)$$

for electrons and ions of charge  $Z$ , respectively (note that for brevity we indicate the magnitude of vectors as scalar variables, e.g.,  $B = |\vec{B}|$ ). A particle with velocity perpendicular to the magnetic field  $v_\perp$  (formally,  $v_\perp = |\vec{v} \times \vec{B}| / B$ ) orbits at its gyroradius,

$$\rho = \frac{v_\perp}{\omega_c} = \frac{mv_\perp}{qB} \quad (1.16)$$

For a thermalized plasma, the perpendicular velocity will, on average, be the thermal velocity  $v_t = \sqrt{2T/m}$ , thus

$$\rho = \frac{\sqrt{2mT}}{qB} \quad (1.17)$$

The introduction of a nonzero electric field drives additional motion for the particle in the form of a drift velocity – the guiding center (that is, the average point about which the orbital motion of the particle gyrates) will shift with a bulk velocity (see [6, § 8.4] for derivation)

$$\vec{v}_d = \frac{\vec{E} \times \vec{B}}{B^2} \quad (1.18)$$

independent of particle charge, mass, or energy.

This restriction of particle motion perpendicular to field lines to short length scales (at fusion-relevant temperatures and magnetic fields, the gyroradius is typically  $\sim 10^{-5}$  m for electrons and  $\sim 10^{-3}$  m for ions) compared to the size of the plasma is central to the concept of magnetic confinement. In the perpendicular direction, this scale restriction of particle motion permits a fluid treatment of the dynamics of the plasma. Further simplification of the fluid model (see [13, § 2.3] for detailed derivation) leads to the theory of *magnetohydrodynamics* (MHD), the “workhorse” model describing plasma behavior. A basic equilibrium in a confined plasma is described in MHD by the simple relation

$$\nabla p = \vec{J} \times \vec{B} \quad (1.19)$$

in which the outward force due to the plasma pressure gradient is balanced by an inward force from the interplay between magnetic fields and electric currents (expressed by the current density  $\vec{J}$ ). This interplay is readily illustrated in the simple one-dimensional case of an infinite straight cylinder of plasma – in this case, the radially-outward  $\nabla p$  force may be balanced by an axial current in the  $\hat{z}$  direction with an azimuthal  $\hat{\theta}$  magnetic field (z-pinch), an azimuthal current and axial field ( $\theta$ -pinch), or a superposition of the two (screw pinch). However, all three of these options suffer from a lack of parallel confinement – as the magnetic field does not restrict the free-streaming parallel motion of the plasma, these linear concepts (when reduced to a physical, non-infinite size!) suffer from plasma losses at the ends of the cylinder. Despite efforts to restrict the parallel motion in a linear device (e.g., the *magnetic mirror*, which pinches the magnetic field at the cylinder ends in order to reflect the parallel motion of particles with a force due to the field gradient [14]), end losses in linear de-

vices proved incompatible with steady-state fusion conditions. The clear solution, then, was to close the magnetic geometry such that the magnetic field lines have no ends: a *torus*.

### 1.2.2 Toroidal Configurations

**Figure 1.4:** Example geometry of a circular-cross-section tokamak plasma, describing a torus of major radius  $R_0$  and minor radius  $a$ , with poloidal coordinate  $\theta$  and toroidal coordinate  $\Phi$ . Tokamak configurations are characterized by an applied toroidal field  $B_T$  with a toroidal plasma current  $I_p$ , which in turn generates a poloidal magnetic field  $B_p$ .



An example toroidal geometry is shown above in fig. 1.4. In comparison to the previous straight cylindrical geometry, the radial coordinate is replaced by a *minor radius*  $r$ , measured from the center of the plasma column to its edge ( $r = a$ ), while the *major radius*  $R_0$  denotes the radius of the torus itself measured from its center axis ( $Z$  in fig. 1.4) to the plasma axis. The azimuthal cylindrical coordinate is replaced by the poloidal coordinate  $\theta$ , wrapping immediately about the plasma column. The axial coordinate in the cylindrical system is replaced by the toroidal angle  $\Phi$  wrapping around the center axis of the torus and describing a circuit along the plasma column. As with the straight cylindrical case, the magnetic geometry may be described with toroidal and poloidal currents and magnetic fields balancing radially-outward thermal pressure.

However, introducing toroidal effects into the magnetic geometry gives rise to additional drift velocities, causing the guiding centers of

particle gyro-orbits to shift (see [6, § 8.5-7]). Spation variation in the magnetic field strength causes the  $\nabla B$  drift, given by

$$\vec{v}_{\nabla B} = \frac{v_{\perp}^2}{2\omega_c} \frac{\vec{B} \times \nabla B}{B^2} \quad (1.20)$$

while the toroidal twist in the magnetic field causes the curvature drift,

$$\vec{v}_k = \frac{v_{\parallel}^2}{\omega_c} \frac{\vec{R}_c \times \vec{B}}{R_c^2 B} \quad (1.21)$$

where  $v_{\parallel}$  is the particle velocity parallel to the magnetic field,  $\omega_c$  is the species cyclotron frequency (eq. (1.15)), and  $\vec{R}_c$  is the radius of curvature of the field. In the case of an applied toroidal magnetic field, these drifts are directed vertically in the  $\hat{Z}$  direction, and are directed oppositely for electrons and ions due to the charge dependence in  $\omega_c$ . The electric field resulting from this charge separation drives an outward  $\vec{E} \times \vec{B}$  drift (see eq. (1.18)), breaking confinement. This effect is countered by the addition of a poloidal field, which adds a helical twist to the guiding-center path to average out the separation due to particle drifts. Concepts aiming for steady-state magnetic confinement of a plasma typically rely on generating this twist, termed the *rotational transform*, to maintain stable confinement.

One of the most successful implementations of this concept for Magnetic Fusion Energy (MFE) is the *tokamak* [7] (a Russian acronym from *тороидальная камера с магнитными катушками*, *toroidalnaya kamera s magnetnymi katushkami*, “toroidal chamber with magnetic coils”). The tokamak design is characterized by a strong toroidal magnetic field (variously denoted  $B_T$  or  $B_\Phi$ ) applied by external coils, with a poloidal field ( $B_p$  or  $B_\theta$ ) primarily generated by a current (termed the *plasma current*  $I_p$ ). A schematic of the plasma and coil arrangement for a tokamak is shown in fig. 1.5. By generating the rotational transform to the magnetic field using the plasma current, the tokamak design utilizes relatively simple planar magnetic coils, avoiding the significantly more complex three-dimensional coils used to generate the helical field in a *stellarator* (the major competing design concept [15]). However, the necessity for large ( $> 1$  MA) plasma currents presents a significant engineering and physics challenge. It is straightforward to generate the plasma current through a simple transformer action from a central solenoid in the torus (depicted in fig. 1.5) – however, this AC-current-driven transformer action necessarily limits tokamaks to pulsed operation. Generation of DC plasma current (via RF or particle beams) is an active area of research in tokamak physics and engineering [7], but is outside the scope of this thesis.

*find section for this  
in Wesson*



**Figure 1.5:** Schematic of a tokamak configuration, showing the plasma and magnetic coils. The applied toroidal magnetic field is generated by the toroidal field coils (shown in blue). A toroidal plasma current is generated by the center transformer, in turn generating a poloidal magnetic field (shown in green). These combine to form the helical magnetic field. The plasma shape and equilibrium is adjusted with the outer poloidal field coils (gray).

Due to its regular, planar magnetic coils and continuous plasma current, tokamak equilibria are characterized by rotational symmetry (to good approximation) about the center axis of the torus (*axisymmetry*). Solutions to the MHD equilibrium equation, eq. (1.19), thus reduce to a two-dimensional equation in  $R$  and  $Z$  (as  $\partial/\partial\Phi \rightarrow 0$ ), given by the Grad-Shafranov Equation [13, 16, 17]:

$$\begin{aligned}\Delta^*\psi &= -\mu_0 R^2 \frac{dp}{d\psi} - \frac{1}{2} \frac{dF^2}{d\psi} \\ \Delta^*\psi &= R^2 \nabla \cdot \left( \frac{1}{R^2} \nabla \psi \right) = R \frac{\partial}{\partial R} \left( \frac{1}{R} \frac{\partial \psi}{\partial R} \right) + \frac{\partial^2 \psi}{\partial Z^2}\end{aligned}\quad (1.22)$$

**Figure 1.6:** Cross-section of a tokamak plasma, illustrating closed magnetic flux surfaces (light blue), the last closed flux surface (red), and surfaces with open magnetic field lines (dark blue). Definitions for plasma shaping parameters elongation  $\kappa$ , and upper and lower triangularity  $\delta_u, \delta_l$  are shown at right.



where  $F = RB_\phi$  encodes the toroidal field and  $p$  is the thermal pressure. The poloidal field (equivalently, the plasma current profile) is described by the poloidal magnetic flux  $\psi$ ,

$$\psi = \frac{1}{2\pi} \int \vec{B}_p \cdot d\vec{S} \quad (1.23)$$

where  $\vec{S}$  is a surface with one edge along the magnetic axis, tracing a contour of constant  $\psi$  when rotated about the axis. In eq. (1.22),  $\psi$  is treated as both an dependent parameter encoding the current, and as an independent variable – a consequence of Grad-Shafranov is that a number of parameters of interest, including pressure and current density, are *flux functions*, constant on a surface of constant  $\psi$ , and thus can be expressed as functions of  $\psi$  alone, e.g.  $p = p(\psi)$ . Moreover, magnetic field lines lie within surfaces of constant flux, with helical structure encoded by the flux function  $q(\psi)$ , termed the *safety factor*, given for a circular cross-section by

$$q = \frac{rB_\Phi}{RB_\theta} \quad (1.24)$$

As the plasma temperature rapidly equilibrates along field lines, the temperature is also a flux function to good approximation. It is useful, then, to picture the confined plasma as a series of closed, nested surfaces of constant  $\psi$ , on which the plasma is trapped (see fig. 1.6). In practice, these contours are calculated via a numerical solution of eq. (1.22) in the EFIT code [18]. For flux functions (i.e., constant

parameters on these flux surfaces), this explicitly removes the dependence on the poloidal angle  $\theta$  – the poloidal flux  $\psi$  is thus a useful one-dimensional abscissa derived directly from the magnetic geometry (thus independent of the physical scale of the tokamak and useful for cross-machine comparisons) for the profiles of most parameters of interest, and shall be used thus for the balance of this thesis.

Using outer poloidal field coils (shown in fig. 1.5), the tokamak operator may push the plasma into a non-circular shape, with beneficial effects on plasma performance and stability. In general, flux surfaces sufficiently far from the plasma core will not close on themselves, instead intersecting the wall; the boundary between closed, nested surfaces and these open surfaces is termed the *last closed flux surface* or LCFS. With sufficient shaping, the operator may generate a null point, the *X-point*, in the LCFS where the poloidal field is zero, splitting the LCFS (also called the *separatrix* in such configurations) into a minimally open surface with “legs” contacting the wall. This magnetic configuration is illustrated in fig. 1.6, along with a diagram defining the typical plasma shaping parameters: elongation  $\kappa$  and upper and lower triangularity  $\delta_u$ ,  $\delta_l$ . As the plasma diffuses outwards, it eventually crosses the LCFS and enters open flux surfaces in the *scrape-off layer* (SOL). The plasma then streams freely along these open magnetic field lines until it contacts the wall. By maintaining an X-point, the operator may steer this plasma exhaust into a section of the tokamak, the *divertor* [7], that is designed to handle this high heat flux – a necessary feature to handle reactor-scale exhaust in a tokamak. •

*find section in  
Wesson*

### 1.3 ALCATOR C-MOD

The data presented in this thesis were collected on the Alcator C-Mod tokamak [19, 20] at the MIT Plasma Science and Fusion Center. The Alcator series of tokamak experiments were designed as compact, high-field tokamaks. Despite its small physical size (67 cm major radius, 22 cm minor radius, considerably smaller than other major experiments), Alcator C-Mod plasmas are capable of reaching ITER- and reactor-relevant densities ( $> 1 \times 10^{20} \text{ m}^{-3}$ ) and pressures ( $> 1 \text{ atm}$ ). This compact design is enabled by a very high toroidal magnetic field driven by liquid-Nitrogen-cooled copper coils, reaching as high as 8.1 T, with typical operation near 5.5 T, allowing reactor-relevant research in a small, cost-effective machine. C-Mod plasmas are primarily heated by ion-cyclotron (ICRF) heating [21], with up to 6 MW of heating power, with an additional  $\sim 1 \text{ MW}$  of lower-hybrid resonance

**Table 1.1:** Summary of Alcator C-Mod typical operating parameters.

parameter	range
major radius	0.67 m
minor radius	0.22 m
toroidal field	3 – 8.1 T
plasma current	$\leq 2 \text{ MA}$
plasma density	$\leq 5 \times 10^{20} \text{ m}^{-3}$
central temperature	$\leq 8 \text{ keV}$
plasma pressure	$\leq 2 \text{ atm}$
ICRF power	6 MW
LHFR power	1 MW

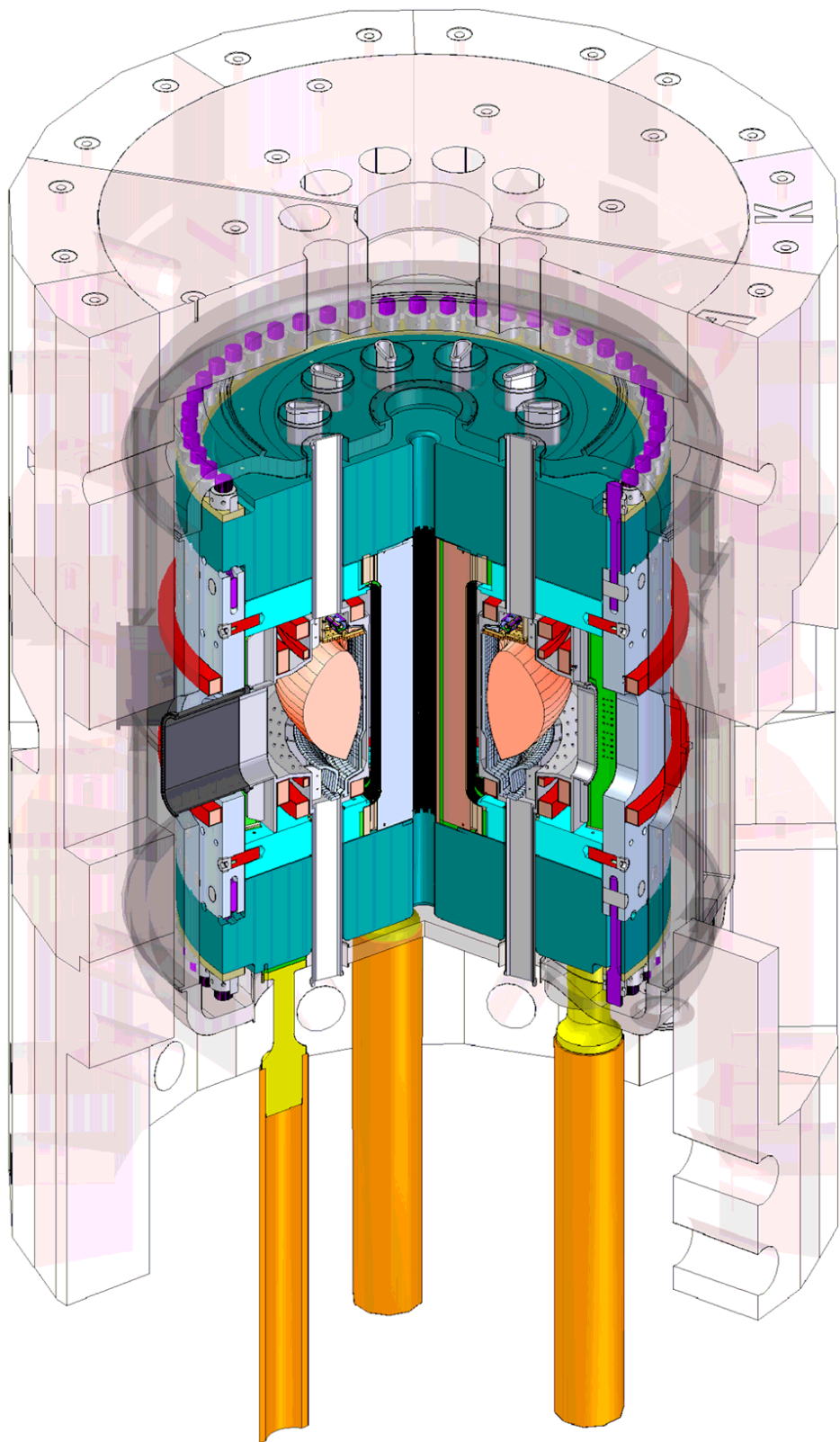


**Figure 1.7:** Cutaway view of the Alcator C-Mod tokamak, including cryostat and ancillary structures, illustrating the extensive support structures necessary for compact, high-field operation.



**Figure 1.8:** Cross-section of the C-Mod vacuum vessel, cryostat and diagnostic access ports, with toroidal-field and equilibrium-field magnetic coils labeled. Also shown is the plasma position in a typical LSN shape, with strike points in the lower divertor shown..

(LHRF) power used for heating and DC current drive [22], providing exceptionally high power density in the  $\sim 1.1 \text{ m}^3$  plasma. A cutaway view of C-Mod, including support structures and the concrete “igloo” housing the cooling systems, is visible in fig. 1.7. A detailed and annotated view of the C-Mod cross-section is shown in fig. 1.8.

Due to their high plasma pressure and power density, C-Mod plasmas must exhaust a large heat flux, reaching levels comparable to that anticipated for ITER [23, 24, 25]. To handle this heat flux, C-Mod operates entirely with high-Z metal materials (primarily Molybdenum and Tungsten) for all plasma-facing surfaces. In addition to its high heat tolerance and low erosion rates due to plasma contact, metal walls provide low retention of fuel gas at the edge – metal walls are thus the leading candidate for ITER- and reactor-scale plasma-facing components.

The presence of a full high-Z lower divertor and upper strike plate, as well as metal limiter walls, gives C-Mod great flexibility in attainable plasma shapes – plasmas may be run in a lower-single null (LSN) shape with the plasma exhaust striking the lower divertor (shown in fig. 1.8, upper-single null (USN) exhausting into the upper strike

plate, or in a limited shape where the scrape-off layer directly impinges on the plasma-facing wall.

## 1.4 CONFINEMENT & TRANSPORT

### 1.4.1 Global Confinement

The rate at which a fusion plasma bleeds off heat is described by a characteristic time scale, the energy confinement time  $\tau_E$ . From basic power balance for the total plasma stored energy  $W_p$ ,

$$\frac{dW_p}{dt} = P_{in} - P_{out} = P_{in} - P_{rad} - \frac{W_p}{\tau_E} \quad (1.25)$$

where  $P_{in}$  is input heating power, from Ohmic heating  $P_{Ohm} = I_p^2 R_{plasma}$ , RF or beam auxiliary heating power  $P_{aux}$ , or self-heating of the plasma from fusion reactions. In the case of the latter, note that as fusion neutrons are immediately lost into the blanket, only the energy carried by *charged* fusion products contributes to fusion self-heating: in the case of D – T fusion we denote this as the alpha heating power  $P_\alpha = 1/5 \times P_{fusion}$  for the energy carried by the  ${}^4\text{He}$  nucleus.  $P_{rad}$  denotes the power loss due to radiative (primarily, Bremsstrahlung) effects, which are considered separately from the transport-driven heat losses encoded by  $W_p/\tau_E$ . It is common to encapsulate these heat source and sink terms into a single net power,

$$P_{net} = P_{Ohm} + P_{aux} + P_{fusion} - P_{rad} - \frac{dW_p}{dt} \quad (1.26)$$

The radiative power loss is occasionally difficult to consistently determine experimentally, is in any case largely independent of operator control (as in the case of auxiliary heating power, or Ohmic power determined by the choice of plasma current) or bulk plasma performance (as in the suppression of turbulent heat losses in high-performance operation), and is relatively negligible at fusion conditions due to its weak scaling with temperature. As such, it is alternately common to express the power as

$$P_{loss} = P_{Ohm} + P_{aux} + P_{fusion} - \frac{dW_p}{dt} \quad (1.27)$$

$$P_{net} = P_{loss} - P_{rad}$$

These definitions allow a simple relation for the experimental energy confinement time,

$$\tau_E = \frac{W_p}{P_{\text{net}}} \quad (1.28)$$

In practice, the physics determining energy confinement are extremely complex; as such, working models for calculating  $\tau_E$  from bulk parameters typically require an empirical power-law scaling.

A closer examination of the power balance equation, eq. (1.25), reveals an important figure of merit. For a DT-burning fusion reactor, steady-state operation with plasma temperatures sustained by fusion self-heating (termed “ignition”) is highly desirable. At these conditions, Bremsstrahlung losses are small, so eq. (1.25) reduces to simply

$$\frac{W_p}{\tau_E} = P_\alpha \quad (1.29)$$

The alpha heating power is simply the fusion reaction rate  $R_f = n_D n_T \langle \sigma v \rangle_{DT}$  times the energy carried by charged particles from a single reaction,  $E_\alpha = 1/5 \times E_{\text{fusion}} = 3.5 \text{ MeV}$ . Quasineutrality (eq. (1.2)) requires  $n_e \approx n_D + n_T$ . As the reaction rate is optimized for a 50-50 fuel mix, the alpha heating power is given by

$$P_\alpha = \frac{1}{4} n_e^2 \langle \sigma v \rangle E_\alpha \quad (1.30)$$

The stored energy is defined by

$$W_p = \frac{3}{2} p_{\text{thermal}} \quad (1.31)$$

with the thermal pressure in the plasma given by

$$p_{\text{thermal}} = n_e T_e + n_D T_D + n_T T_T = 2n_e T_e \quad (1.32)$$

assuming the condition above on the electron and ion densities, and assuming temperature equilibration  $T_e \approx T_D \approx T_T$ . This, then, implies  $W_p = 3n_e T_e$  (a convenient expression, as electron quantities are typically more readily measured in plasma experiments). Power balance at ignition then requires

$$\frac{3n_e T_e}{\tau_E} = \frac{1}{4} n_e^2 \langle \sigma v \rangle E_\alpha \quad (1.33)$$

thus simplifying to the Lawson Criterion [26]

$$n_e \tau_E = \frac{12 T_e}{\langle \sigma v \rangle E_\alpha} \quad (1.34)$$

Scaling both sides by  $2T_e$  gives the “triple product,”

$$2n_e T_e \tau_E = p \tau_E = \frac{24 T_e^2}{\langle \sigma v \rangle E_\alpha} \quad (1.35)$$

an important figure of merit for a reactor that is optimized at  $T_e \approx 15 \text{ keV}$  with a value of  $p \tau_E \approx 8.3 \text{ atm} \cdot \text{s}$ , setting target parameters for a fusion reactor [15].

However, the maximum attainable thermal pressure in a tokamak is limited by a global MHD stability limit expressed in terms of the normalized pressure [7, § 6.16]

$$\beta = \frac{2\mu_0 p}{B^2} \quad (1.36)$$

which encodes the ratio of thermal pressure to magnetic pressure  $B^2/2\mu_0$  (equivalently, the ratio of thermal and magnetic stored energy) – a normalization that also falls naturally out of solutions to the MHD equilibrium, eq. (1.19). Although the maximum stable pressure may be increased with higher plasma current and toroidal field (motivating high-field design for tokamaks), reactor-scale operation requires increased energy confinement – that is, higher values for  $\tau_E$  – to reach the triple-product target.

#### 1.4.2 Transport Barriers

*how deep to go with this?*

Global improvement to energy confinement may be achieved through local modification of the transport of energy or particles out of the plasma, achieved via structures termed *transport barriers*. While the physics driving the formation of transport barriers is not entirely understood, the effect is evidently caused by sheared flows in the plasma – these break up the turbulent “eddies” driving much of the energy or particle transport through the plasma, locally reducing transport drive in the sheared region.

The effect on the transport is clearly evident from a diffusive transport model, given by

$$\frac{\partial Q}{\partial t} = \nabla \cdot (D_Q \nabla Q) + R_Q \quad (1.37)$$

for a general parameter  $Q(\vec{x}, t)$  with accompanying diffusion coefficient  $D_Q(Q, \vec{x}, t)$  and net source/sink term  $R_Q(Q, \vec{x}, t)$ . We may consider a one-dimensional “toy model” of diffusion with a simple constant source term, given in steady state by

$$\frac{d}{dx} \left( D_Q \frac{dQ}{dx} \right) + R_Q = 0 \quad (1.38)$$

The solution to this model for two sample diffusion coefficients is given in fig. 1.9. A simple constant diffusion coefficient  $D_Q$  produces a profile with weak slope, whereas an order-of-magnitude drop in  $D_Q$  near the edge (consistent with experimentally-observed values of diffusion coefficients in transport barriers) produces a region with a steep gradient in  $Q$  compared to the flat- $D_Q$  solution, despite identical source terms  $R_Q$ . Experimentally, reductions in the particle transport coefficient  $D_n$  or the heat transport coefficient  $\chi$  due to sheared flows correspond to steep-gradient regions in density or temperature, characteristic of the transport barrier.

Of particular interest is the *edge transport barrier*, also termed the *pedestal* [27, 28]. A number of high-performance tokamak regimes have been established, exploiting the formation of a pedestal to suppress transport and boost global energy confinement to levels necessary to reach the triple-product target (eq. (1.35)) for an ignited plasma. The understanding of these high-performance regimes, commonly referred to as “high-confinement” or H-modes, and their extrapolation to ITER and reactor-scale devices has been a major focus of recent tokamak research.

However, the formation of the pedestal also presents challenges that must be addressed for reactor-scale operation. Increased particle confinement causes the plasma to retain impurities – particularly ionized wall materials – along with fuel ions. These impurities both dilute the fuel, slowing the fusion reaction rate, and drive elevated radiative losses due to their higher nuclear charge (note the strong charge dependence in eq. (1.6)). This ultimately leads to a *radiative collapse*, dropping the plasma out of H-mode – thus, stationary (i.e., non-transient) operation in H-mode requires a means to regulate particle confinement and flush impurities from the plasma core.



**Figure 1.9:** Diffusion coefficients and plasma profiles for a “toy model” 1D diffusion equation with a general parameter  $Q(x)$  and accompanying diffusion coefficient  $D_Q(x)$ .

*show equation for  
this?*

*cite for this?*

The steep gradient in the plasma pressure generated in the pedestal has been shown to drive *Edge-Localized Modes* (ELMs) [29], instabilities that cause the pedestal to periodically “crash,” expelling particles and energy into the scrape-off layer. The smaller ELM bursts found in existing experiments provide the desired level of particle transport for stationary operation – thus ITER operation is designed considering an H-mode with ELMs as the baseline for operation [30, 31]. However, on ITER-scale devices the heat pulses from ELMs drive unacceptable levels of transient thermal loading and erosion damage to wall and divertor materials [32, 33]. As such, high-performance operation on ITER- or reactor-scale devices requires mitigation or elimination of large, deleterious ELMs, either through externally-applied controls or physics-based stabilization.

•

## 1.5 GOALS & OUTLINE

This thesis will present results in the *I-mode*, a novel high-performance regime pioneered on Alcator C-Mod. I-mode is notable for its apparent decoupling of energy and particle transport, reaching H-mode-like energy confinement while maintaining L-mode levels of particle and impurity transport, achieving the desired flushing of impurities from the plasma. This manifests in the edge with the formation of an H-mode-like temperature pedestal without the accompanying density pedestal found in conventional H-modes. I-mode also appears to be naturally free of large ELMs, avoiding the need for complex externally-applied controls, and to exhibit highly favorable scalings of energy confinement with heating power.

reward this

A firm understanding of the structure and stability of the pedestal is essential to extend I-mode operation to larger devices. This thesis will describe a combined approach to the understanding of the pedestal in I-mode, using both direct observations of pedestal structure and numerical modeling of the pedestal stability against identified triggers for large, deleterious ELMs, to better establish the operating space and reliability of I-mode for reactor operation. The balance of the thesis is arranged as follows:

### CHAPTER 2: HIGH-PERFORMANCE REGIMES

An overview of existing results in established H-mode regimes, including observed pedestal behaviors. A detailed introduction to I-mode physics and operation is also included.

### CHAPTER 3: PEDESTAL MODELING AND THEORY

An introduction to the theory of the MHD and turbulent instabilities governing the pedestal and driving large ELMs, and the numerical modeling approaches used in their analysis.

### CHAPTER 4: ELMY H-MODES ON C-MOD

The results of recent experiments on C-Mod testing a unified

model for pedestal structure in ELM<sub>H</sub> mode, the approach to which is also applied to I-mode pedestals.

**CHAPTER 5: I-MODE PEDESTAL SCALINGS**

New results from dedicated pedestal experiments in I-mode examining the response of pedestal structure to engineering and physics parameters, and potential extrapolations of pedestal structure and performance to larger devices.

**CHAPTER 6: I-MODE PEDESTAL STABILITY MODELING**

Numerical modeling results for the stability of I-mode pedestals against identified ELM triggers, and correlations to the generally observed lack of ELMs in I-mode.

**CHAPTER 7: CONCLUSIONS**

A summary of the results presented in this thesis and some directions for future work.

An overview of the diagnostics used in the experiments presented here is also given in appendix A. \*



## BIBLIOGRAPHY

---

- [1] United Nations. *World Population Prospects: The 2010 Revision. Comprehensive Tables*, volume 1. United Nations, 2010.
- [2] J. Klugman et al. *Human development report 2011. Sustainability and Equity: A Better Future for All*, 2011.
- [3] H. Gruenspecht. *International energy outlook 2011. Center for Strategic and International Studies*, 2010.
- [4] B.P. Global. *Statistical review of world energy 2010*.
- [5] U.S. Energy Information Administration. *Annual coal report 2012*, 2013.
- [6] J.P. Freidberg. *Plasma Physics and Fusion Energy*. Cambridge books online. Cambridge University Press, 2007.
- [7] J. Wesson. *Tokamaks*. International Series of Monographs on Physics. Oxford University Press, 2011.
- [8] F.F. Chen. *Introduction to Plasma Physics and Controlled Fusion*. Springer, 1984.
- [9] K.S. Krane. *Introductory Nuclear Physics*. Wiley, 1987.
- [10] W.M. Haynes. *CRC Handbook of Chemistry and Physics, 93rd Edition*. Taylor & Francis, 2012.
- [11] WenZhe Fa and YaQiu Jin. *Global inventory of Helium-3 in lunar regoliths estimated by a multi-channel microwave radiometer on the Chang-E 1 lunar satellite*. *Chinese Science Bulletin*, 55(35):4005–4009, 2010.
- [12] B. Palaszewski. *Atmospheric mining in the outer solar system*. In *41st American Institute of Aeronautics and Astronautics Joint Propulsion Conference and Exhibit*, 2005.
- [13] Jeffrey P. Freidberg. *Ideal Magnetohydrodynamics*. Springer, 1987.
- [14] J. Kesner, R.S. Post, B.D. McVey, and D.K. Smith. *A tandem mirror with axisymmetric central-cell ion confinement*. *Nuclear Fusion*, 22(4):549, 1982.
- [15] Dale Meade. *50 years of fusion research*. *Nuclear Fusion*, 50(1):014004, 2010.

- [16] H. Grad and H. Rubin. MHD equilibrium in an axisymmetric toroid. In *Proceedings of the 2nd U.N. Conference on the Peaceful Uses of Atomic Energy*, volume 31, page 190, 1958.
- [17] V.D. Shafranov. Grad-Shafranov equation for MHD equilibrium in a torus. *Soviet Physics, Journal of Experimental and Theoretical Physics*, 26:682, 1960.
- [18] L.L. Lao, H. St. John, R.D. Stambaugh, A.G. Kellman, and W. Pfeiffer. **Reconstruction of current profile parameters and plasma shapes in tokamaks.** *Nuclear Fusion*, 25(11):1611, 1985.
- [19] I. H. Hutchinson, R. Boivin, F. Bombarda, P. Bonoli, S. Fairfax, C. Fiore, J. Goetz, S. Golovato, R. Granetz, M. Greenwald, S. Horne, A. Hubbard, J. Irby, B. LaBombard, B. Lipschultz, E. Marmar, G. McCracken, M. Porkolab, J. Rice, J. Snipes, Y. Takase, J. Terry, S. Wolfe, C. Christensen, D. Garnier, M. Graf, T. Hsu, T. Luke, M. May, A. Niemczewski, G. Tinios, J. Schachter, and J. Urbahn. **First results from Alcator C-Mod.** *Physics of Plasmas*, 1(5):1511–1518, 1994.
- [20] M. Greenwald, N. Basse, P. Bonoli, R. Bravenec, E. Edlund, D. Ernst, C. Fiore, R. Granetz, A. Hubbard, J. Hughes, I. Hutchinson, J. Irby, B. LaBombard, L. Lin, Y. Lin, B. Lipschultz, E. Marmar, D. Mikkelsen, D. Mossessian, P. Phillips, M. Porkolab, J. Rice, W. Rowan, S. Scott, J. Snipes, J. Terry, S. Wolfe, S. Wukitch, and K. Zhurovich. **Confinement and transport research in Alcator C-Mod.** *Fusion Science and Technology*, 51(3):266–287, 2007.
- [21] Y. Takase, R. L. Boivin, F. Bombarda, P. T. Bonoli, C. L. Fiore, D. Garnier, J. A. Goetz, S. N. Golovato, R. S. Granetz, M. J. Greenwald, S. F. Horne, A. E. Hubbard, I. H. Hutchinson, J. H. Irby, H. Kimura, R. Majeski, E. S. Marmar, M. May, A. Mazurenko, P. O'Shea, R. Pinsker, M. Porkolab, J. Reardon, J. E. Rice, C. Rost, J. Schachter, J. A. Snipes, P. Stek, J. L. Terry, R. L. Watterson, B. Welch, and S. M. Wolfe. **Survey of ICRF heating experiments and enhanced performance modes in Alcator C-Mod.** *Plasma Physics and Controlled Fusion*, 38(12):2215, 1996.
- [22] J.R. Wilson, R. Parker, M. Bitter, P.T. Bonoli, C. Fiore, R.W. Harvey, K. Hill, A.E. Hubbard, J.W. Hughes, A. Ince-Cushman, C. Kessel, J.S. Ko, O. Meneghini, C.K. Phillips, M. Porkolab, J. Rice, A.E. Schmidt, S. Scott, S. Shiraiwa, E. Valeo, G. Wallace, J.C. Wright, and the Alcator C-Mod Team. **Lower hybrid heating and current drive on the Alcator C-Mod tokamak.** *Nuclear Fusion*, 49(11):115015, 2009.
- [23] A. Loarte, B. Lipschultz, A.S. Kukushkin, G.F. Matthews, P.C. Stangeby, N. Asakura, G.F. Counsell, G. Federici, A. Kallenbach,

- K. Krieger, A. Mahdavi, V. Philipps, D. Reiter, J. Roth, J. Strachan, D. Whyte, R. Doerner, T. Eich, W. Fundamenski, A. Hermann, M. Fenstermacher, P. Ghendrih, M. Groth, A. Kirschner, S. Konoshima, B. LaBombard, P. Lang, A.W. Leonard, P. Monier-Garbet, R. Neu, H. Pacher, B. Pegourie, R.A. Pitts, S. Takamura, J. Terry, E. Tsitrone, the ITPA Scrape-off Layer, and Divertor Physics Topical Group. **Chapter 4: Power and particle control.** *Nuclear Fusion*, 47(6):S203, 2007.
- [24] J. L. Terry, B. LaBombard, B. Lipschultz, M. J. Greenwald, J. E. Rice, and S. J. Zweben. **The scrape-off layer in Alcator C-Mod: Transport, turbulence, and flows.** *Fusion Science and Technology*, 51(3):342–356, 2007.
- [25] B. LaBombard, J. L. Terry, J. W. Hughes, D. Brunner, J. Payne, M. L. Reinke, I. Cziegler, R. Granetz, M. Greenwald, I. H. Hutchinson, J. Irby, Y. Lin, B. Lipschultz, Y. Ma, E. S. Marmar, W. L. Rowan, N. Tsujii, G. Wallace, D. G. Whyte, S. Wolfe, S. Wukitch, G. Wurden, and Alcator C-Mod Team. **Scaling of the power exhaust channel in Alcator C-Mod.** *Physics of Plasmas*, 18(5):056104, 2011.
- [26] J D Lawson. **Some criteria for a power producing thermonuclear reactor.** *Proceedings of the Physical Society. Section B*, 70(1):6, 1957.
- [27] F. Wagner, G. Becker, K. Behringer, D. Campbell, A. Eberhagen, W. Engelhardt, G. Fussmann, O. Gehre, J. Gernhardt, G. v. Gierke, G. Haas, M. Huang, F. Karger, M. Keilhacker, O. Klüber, M. Kornherr, K. Lackner, G. Lisitano, G. G. Lister, H. M. Mayer, D. Meisel, E. R. Müller, H. Murmann, H. Niemann, W. Poschenrieder, H. Rapp, H. Röhr, F. Schneider, G. Siller, E. Speth, A. Stäbler, K. H. Steuer, G. Venus, O. Vollmer, and Z. Yü. **Regime of improved confinement and high beta in neutral-beam-heated divertor discharges of the ASDEX tokamak.** *Phys. Rev. Lett.*, 49(19):1408–1412, Nov 1982.
- [28] M. Greenwald, R.L. Boivin, F. Bombarda, P.T. Bonoli, C.L. Fiore, D. Garnier, J.A. Goetz, S.N. Golovato, M.A. Graf, R.S. Granetz, S. Horne, A. Hubbard, I.H. Hutchinson, J.H. Irby, B. LaBombard, B. Lipschultz, E.S. Marmar, M.J. May, G.M. McCracken, P. O’Shea, J.E. Rice, J. Schachter, J.A. Snipes, P.C. Stek, Y. Takase, J.L. Terry, Y. Wang, R. Watterson, B. Welch, and S.M. Wolfe. **H-mode confinement in Alcator C-Mod.** *Nuclear Fusion*, 37(6):793, 1997.
- [29] H Zohm. **Edge localized modes (ELMs).** *Plasma Physics and Controlled Fusion*, 38(2):105, 1996.
- [30] ITER Physics Expert Group on Confinement, Transport and ITER Physics Expert Group on Confinement Modelling and Database,

- and ITER Physics Basis Editors. **Chapter 2: Plasma confinement and transport.** *Nuclear Fusion*, 39(12):2175, 1999.
- [31] M. Shimada, D.J. Campbell, V. Mukhovatov, M. Fujiwara, N. Kirneva, K. Lackner, M. Nagami, V.D. Pustovitov, N. Uckan, J. Wesley, N. Asakura, A.E. Costley, A.J.H. Donné, E.J. Doyle, A. Fasoli, C. Gormezano, Y. Gribov, O. Gruber, T.C. Hender, W. Houlberg, S. Ide, Y. Kamada, A. Leonard, B. Lipschultz, A. Loarte, K. Miyamoto, V. Mukhovatov, T.H. Osborne, A. Polevoi, and A.C.C. Sips. **Chapter 1: Overview and summary.** *Nuclear Fusion*, 47(6):S1, 2007.
- [32] A Loarte, G Saibene, R Sartori, D Campbell, M Becoulet, L Horton, T Eich, A Herrmann, G Matthews, N Asakura, A Chankin, A Leonard, G Porter, G Federici, G Janeschitz, M Shimada, and M Sugihara. **Characteristics of type I ELM energy and particle losses in existing devices and their extrapolation to ITER.** *Plasma Physics and Controlled Fusion*, 45(9):1549, 2003.
- [33] G Federici, A Loarte, and G Strohmayer. **Assessment of erosion of the ITER divertor targets during type I ELMs.** *Plasma Physics and Controlled Fusion*, 45(9):1523, 2003.

# 2

## HIGH-PERFORMANCE REGIMES

---

The development of magnetic-confinement fusion into an economical form of power generation is characterized by two seemingly contrary requirements: first, a high level of energy confinement is necessary to reach the desired level of self-heating of the plasma by fusion products, satisfying triple-product requirements (eq. (1.35)). At the same time, particle transport must be sufficient to avoid the deleterious effects of accumulated helium “fusion ash” and other impurities on fusion performance – particularly important in the case of the high-Z impurities from the metal plasma-facing walls necessary for reactor-scale devices [1].

[more cites?](#)

A number of operating scenarios, collectively termed “high confinement” or H-modes[2], satisfying these requirements have been developed. The “low confinement” or L-mode operating baseline of energy confinement, characterized through an extensive multi-machine scaling study [3] by the ITER-89 scaling,

$$\tau_{E,ITER89} = 0.048 \times \bar{n}_e^{0.1} M^{0.5} I_p^{0.85} R^{1.2} a^{0.3} \kappa^{0.5} B_T^{0.2} P_{aux}^{-0.5} \quad (2.1)$$

in which  $\bar{n}_e$  is the line-averaged density ( $10^{20} \text{ m}^{-3}$ ),  $M$  is the atomic mass (amu),  $I_p$  is the plasma current (MA),  $B_T$  is the toroidal field (T),  $R$  and  $a$  are the major and minor radii in m (see fig. 1.4),  $\kappa$  is the elongation (see fig. 1.6), and  $P_{aux}$  is the externally-applied heating power (MW). Compared to this baseline, H-modes represent a significant improvement in performance, with confinement – here represented in a normalized sense by the H-factor, i.e.,

$$H_{89} = \frac{\tau_E}{\tau_{E,ITER89}} \quad (2.2)$$

by at least a factor of two.

[more specific, cites?](#)

### 2.1 ELM-FREE H-MODE



**Table 2.1:** Typical operating parameters of tokamaks noted in this thesis, with reference to overviews. Note: all ITER values are projected.[check all values here](#)

Device	R/a [m]	I_p [MA]	B_T [T]	$\bar{n}_e$ [ $m^{-3}$ ]	T_e0 [keV]	refs
C-Mod (USA)	0.67/0.22	$\leq 2$	3 – 8.1	$\leq 5 \times 10^{20}$	$\leq 8$	[4, 5, 6]
DIII-D (USA)	1.67/0.67	1 – 3	2.2	$6 \times 10^{19}$	5 – 10	[7, 8, 9]
ASDEX-U (GER)	1.65/0.5	$\sim 1$	3.9	$7.5 \times 10^{19}$	2 – 3	[10, 11, 12]
JET (UK)	3.4/0.9	3 – 4	3.8	$5 \times 10^{19}$	10 – 20	[13, 14]
JT-60U (JAP)	3.4/0.9	3 – 4	4.8	$5 \times 10^{19}$	10 – 20	[15, 16]
JFT-2M (JAP)	1.3/0.35	0.5	2.2	$5 \times 10^{19}$	1 – 2	[17, 18]
ITER*	6.2/2.0	15	5.3	$1 \times 10^{20}$	10	[19, 20]

## 2.2 ELMY H-MODE

### 2.2.1 Global Parameters

### 2.2.2 Fluctuations and ELMs

### 2.2.3 Active ELM Control

•

## 2.3 ELM-SUPPRESSED H-MODES

### 2.3.1 QH-Mode

### 2.3.2 EDA H-Mode

•

## 2.4 I-MODE

### 2.4.1 Access and Operation

### 2.4.2 Global Performance

### 2.4.3 Edge Fluctuations – the Weakly-Coherent Mode

★

## BIBLIOGRAPHY

---

- [1] A. Loarte, B. Lipschultz, A.S. Kukushkin, G.F. Matthews, P.C. Stangeby, N. Asakura, G.F. Counsell, G. Federici, A. Kallenbach, K. Krieger, A. Mahdavi, V. Philipps, D. Reiter, J. Roth, J. Strachan, D. Whyte, R. Doerner, T. Eich, W. Fundamenski, A. Herrmann, M. Fenstermacher, P. Ghendrih, M. Groth, A. Kirschner, S. Konoshima, B. LaBombard, P. Lang, A.W. Leonard, P. Monier-Garbet, R. Neu, H. Pacher, B. Pegourie, R.A. Pitts, S. Takamura, J. Terry, E. Tsitrone, the ITPA Scrape-off Layer, and Divertor Physics Topical Group. **Chapter 4: Power and particle control.** *Nuclear Fusion*, 47(6):S203, 2007.
- [2] F. Wagner, G. Becker, K. Behringer, D. Campbell, A. Eberhagen, W. Engelhardt, G. Fussmann, O. Gehre, J. Gernhardt, G. v. Gierke, G. Haas, M. Huang, F. Karger, M. Keilhacker, O. Klüber, M. Kornherr, K. Lackner, G. Lisitano, G. G. Lister, H. M. Mayer, D. Meisel, E. R. Müller, H. Murmann, H. Niemann, W. Poschenrieder, H. Rapp, H. Röhr, F. Schneider, G. Siller, E. Speth, A. Stäbler, K. H. Steuer, G. Venus, O. Vollmer, and Z. Yü. **Regime of improved confinement and high beta in neutral-beam-heated divertor discharges of the ASDEX tokamak.** *Phys. Rev. Lett.*, 49(19):1408–1412, Nov 1982.
- [3] P.N. Yushmanov, T. Takizuka, K.S. Riedel, O.J.W.F. Kardaun, J.G. Cordey, S.M. Kaye, and D.E. Post. **Scalings for tokamak energy confinement.** *Nuclear Fusion*, 30(10):1999, 1990.
- [4] I. H. Hutchinson, R. Boivin, F. Bombarda, P. Bonoli, S. Fairfax, C. Fiore, J. Goetz, S. Golovato, R. Granetz, M. Greenwald, S. Horne, A. Hubbard, J. Irby, B. LaBombard, B. Lipschultz, E. Marmar, G. McCracken, M. Porkolab, J. Rice, J. Snipes, Y. Takase, J. Terry, S. Wolfe, C. Christensen, D. Garnier, M. Graf, T. Hsu, T. Luke, M. May, A. Niemczewski, G. Tinios, J. Schachter, and J. Urbahn. **First results from Alcator C-Mod.** *Physics of Plasmas*, 1(5):1511–1518, 1994.
- [5] M. Greenwald, N. Basse, P. Bonoli, R. Bravenec, E. Edlund, D. Ernst, C. Fiore, R. Granetz, A. Hubbard, J. Hughes, I. Hutchinson, J. Irby, B. LaBombard, L. Lin, Y. Lin, B. Lipschultz, E. Marmar, D. Mikkelsen, D. Mossessian, P. Phillips, M. Porkolab, J. Rice, W. Rowan, S. Scott, J. Snipes, J. Terry, S. Wolfe, S. Wukitch, and K. Zhurovich. **Confinement and transport research in Alcator C-Mod.** *Fusion Science and Technology*, 51(3):266–287, 2007.

- [6] M. Greenwald, A. Bader, S. Baek, H. Barnard, W. Beck, W. Bergerson, I. Bespamyatnov, M. Bitter, P. Bonoli, M. Brookman, D. Brower, D. Brunner, W. Burke, J. Candy, M. Chilenski, M. Chung, M. Churchill, I. Cziegler, E. Davis, G. Dekow, L. Delgado-Aparicio, A. Diallo, W. Ding, A. Dominguez, R. Ellis, P. Ennever, D. Ernst, I. Faust, C. Fiore, E. Fitzgerald, T. Fredian, O.E. Garcia, C. Gao, M. Garrett, T. Golfinopoulos, R. Granetz, R. Groebner, S. Harrison, R. Harvey, Z. Hartwig, K. Hill, J. Hillairet, N. Howard, A.E. Hubbard, J.W. Hughes, I. Hutchinson, J. Irby, A.N. James, A. Kanojia, C. Kasten, J. Kesner, C. Kessel, R. Kube, B. LaBombard, C. Lau, J. Lee, K. Liao, Y. Lin, B. Lipschultz, Y. Ma, E. Marmar, P. McGibbon, O. Meneghini, D. Mikkelsen, D. Miller, R. Mumgaard, R. Murray, R. Ochoukov, G. Olynyk, D. Pace, S. Park, R. Parker, Y. Podpaly, M. Porkolab, M. Preynas, I. Pusztai, M. Reinke, J. Rice, W. Rowan, S. Scott, S. Shiraiwa, J. Sierchio, P. Snyder, B. Sorbom, V. Soukhanovskii, J. Stillerman, L. Sugiyama, C. Sung, D. Terry, J. Terry, C. Theiler, N. Tsujii, R. Vieira, J. Walk, G. Wallace, A. White, D. Whyte, J. Wilson, S. Wolfe, K. Woller, G. Wright, J. Wright, S. Wukitch, G. Wurden, P. Xu, C. Yang, and S. Zweben. **Overview of experimental results and code validation activities at Alcator C-Mod.** *Nuclear Fusion*, 53(10):104004, 2013.
- [7] J.L. Luxon. **A design retrospective of the DIII-D tokamak.** *Nuclear Fusion*, 42(5):614, 2002.
- [8] J.L. Luxon, T.C. Simonen, R.D. Stambaugh, and the DIII-D Team. **Overview of the DIII-D fusion science program.** *Fusion Science and Technology*, 48(2):807–827, October 2005.
- [9] J.L. Luxon. **A brief introduction to the DIII-D tokamak.** *Fusion Science and Technology*, 48(2):828–833, October 2005.
- [10] A. Herrmann and O. Gruber. **Chapter 1: ASDEX upgrade - introduction and overview.** *Fusion Science and Technology*, 44(3):569–577, November 2003.
- [11] F. Ryter, A. Stäbler, and G. Tardini. **Chapter 5: Core energy transport in conventional scenarios in ASDEX upgrade.** *Fusion Science and Technology*, 44(3):618–635, November 2003.
- [12] U. Stroth, J. Adamek, L. Aho-Mantila, S. Äkäslompolo, C. Amador, C. Angioni, M. Balden, S. Bardin, L. Barrera Orte, K. Behler, E. Belonohy, A. Bergmann, M. Bernert, R. Bilato, G. Birkenmeier, V. Bobkov, J. Boom, C. Bottreau, A. Bottino, F. Braun, S. Brezinsek, T. Brochard, M. Brüdgam, A. Buhler, A. Burckhart, F.J. Casson, A. Chankin, I. Chapman, F. Clairet, I.G.J. Classen, J.W. Coenen, G.D. Conway, D.P. Coster, D. Curran, F. da Silva, P. de Marné, R. D'Inca, D. Douai, R. Drube, M. Dunne, R. Dux,

T. Eich, H. Eixenberger, N. Endstrasser, K. Engelhardt, B. Esposto, E. Fable, R. Fischer, H. Fünfgelder, J.C. Fuchs, K. Gál, M. García Muñoz, B. Geiger, L. Giannone, T. Görler, S. da Graca, H. Greuner, O. Gruber, A. Gude, L. Guimarais, S. Günter, G. Haas, A.H. Hakola, D. Hangan, T. Happel, T. Härtl, T. Hauff, B. Heinemann, A. Herrmann, J. Hobirk, H. Höhnle, M. Hözl, C. Hopf, A. Houben, V. Igochine, C. Ionita, A. Janzer, F. Jenko, M. Kantor, C.-P. Käsemann, A. Kallenbach, S. Kálvin, M. Kantor, A. Kappatou, O. Kardaun, W. Kasparek, M. Kaufmann, A. Kirk, H.-J. Klingshirn, M. Kocan, G. Kocsis, C. Konz, R. Koslowski, K. Krieger, M. Kubic, T. Kurki-Suonio, B. Kurzan, K. Lackner, P.T. Lang, P. Lauber, M. Laux, A. Lazaros, F. Leipold, F. Leuterer, S. Lindig, S. Lisgo, A. Lohs, T. Lunt, H. Maier, T. Makkonen, K. Mank, M.-E. Manso, M. Maraschek, M. Mayer, P.J. McCarthy, R. McDermott, F. Mehlmann, H. Meister, L. Menchero, F. Meo, P. Merkel, R. Merkel, V. Mertens, F. Merz, A. Mlynek, F. Monaco, S. Müller, H.W. Müller, M. Münich, G. Neu, R. Neu, D. Neuwirth, M. Nocente, B. Nold, J.-M. Noterdaeme, G. Pautasso, G. Pereverzev, B. Plöckl, Y. Podoba, F. Pompon, E. Poli, K. Polozhiy, S. Potzel, M.J. Püschel, T. Pütterich, S.K. Rathgeber, G. Raupp, M. Reich, F. Reimold, T. Ribeiro, R. Riedl, V. Rohde, G. v. Rooij, J. Roth, M. Rott, F. Ryter, M. Salewski, J. Santos, P. Sauter, A. Scarabosio, G. Schall, K. Schmid, P.A. Schneider, W. Schneider, R. Schrittweiser, M. Schubert, J. Schweinzer, B. Scott, M. Sempf, M. Sertoli, M. Siccinio, B. Sieglin, A. Sigalov, A. Silva, F. Sommer, A. Stäbler, J. Stober, B. Streibl, E. Strumberger, K. Sugiyama, W. Suttrop, T. Tala, G. Tardini, M. Teschke, C. Tichmann, D. Told, W. Treutterer, M. Tsallas, M. A. Van Zeeland, P. Varela, G. Veres, J. Vicente, N. Vianello, T. Vierle, E. Viezzer, B. Viola, C. Vorpahl, M. Wachowski, D. Wagner, T. Wauters, A. Weller, R. Wenninger, B. Wieland, M. Willendorfer, M. Wischmeier, E. Wolfrum, E. Würsching, Q. Yu, I. Zammuto, D. Zasche, T. Zehetbauer, Y. Zhang, M. Zilker, and H. Zohm. **Overview of ASDEX upgrade results.** *Nuclear Fusion*, 53(10):104003, 2013.

- [13] D.C. McDonald, Y. Andrew, G.T.A. Huysmans, A. Loarte, J. Onenga, J. Rapp, and S. Saarelma. **Chapter 3: ELMy H-mode operation on JET.** *Fusion Science and Technology*, 53(4):891–957, May 2008.
- [14] F. Romanelli and JET EFDA Contributors. **Overview of the JET results with the ITER-like wall.** *Nuclear Fusion*, 53(10):104002, 2013.
- [15] Y. Kamada, T. Fujita, S. Ishida, M. Kikuchi, S. Ide, T. Takizuka, H. Shirai, Y. Koide, T. Fukuda, N. Hosogane, K. Tsuchiya, T. Hatae, H. Takenaga, M. Sato, H. Nakamura, O. Naito,

- N. Asakura, H. Kubo, S. Higashijima, Y. Miura, R. Yoshino, K. Shimizu, T. Ozeki, T. Hirayama, M. Mori, Y. Sakamoto, Y. Kawano, A. Isayama, K. Ushigusa, Y. Ikeda, H. Kimura, T. Fujii, T. Imai, M. Nagami, S. Takeji, T. Oikawa, T. Suzuki, T. Nakano, N. Oyama, S. Sakurai, S. Konoshima, T. Sugie, K. Tobita, T. Kondoh, H. Tamai, Y. Neyatani, A. Sakasai, Y. Kusama, K. Itami, M. Shimada, H. Ninomiya, and H. Urano. **Fusion plasma performance and confinement studies on JT-60 and JT-60U.** *Fusion Science and Technology*, 42(2,3):185–254, November 2002.
- [16] A. Kitsunezaki, M. Shimizu, H. Ninomiya, M. Kuriyama, and the JT-60 Team. **JT-60 program.** *Fusion Science and Technology*, 42(2,3):179–184, September 2002.
- [17] Y. Kusama, M. Yamamoto, and the JFT-2M Group. **JFT-2M program.** *Fusion Science and Technology*, 49(2):89–95, February 2006.
- [18] Y. Miura, M. Mori, T. Shoji, H. Matsumoto, K. Kamiya, K. Ida, and S. Kasai. **Studies of improved confinement in JFT-2M.** *Fusion Science and Technology*, 49(2):96–121, February 2006.
- [19] M. Shimada, D.J. Campbell, V. Mukhovatov, M. Fujiwara, N. Kirneva, K. Lackner, M. Nagami, V.D. Pustovitov, N. Uckan, J. Wesley, N. Asakura, A.E. Costley, A.J.H. Donné, E.J. Doyle, A. Fasoli, C. Gormezano, Y. Gribov, O. Gruber, T.C. Hender, W. Houlberg, S. Ide, Y. Kamada, A. Leonard, B. Lipschultz, A. Loarte, K. Miyamoto, V. Mukhovatov, T.H. Osborne, A. Polevoi, and A.C.C. Sips. **Chapter 1: Overview and summary.** *Nuclear Fusion*, 47(6):S1, 2007.
- [20] ITER Physics Expert Group on Confinement, Transport and ITER Physics Expert Group on Confinement Modelling and Database, and ITER Physics Basis Editors. **Chapter 2: Plasma confinement and transport.** *Nuclear Fusion*, 39(12):2175, 1999.

# 3

## PEDESTAL MODELING AND THEORY

---

introduce!

### 3.1 EMPIRICAL MODELS



### 3.2 MHD STABILITY: PEELING-BALLOONING MODES

#### 3.2.1 *Ballooning MHD*

#### 3.2.2 *Peeling MHD*

#### 3.2.3 *ELITE Code*



### 3.3 TURBULENT MODELING



### 3.4 THE EPED MODEL





## BIBLIOGRAPHY

---



# 4

## ELMY H-MODES ON C-MOD

---

### 4.1 ELMY H-MODES ACCESS

•

### 4.2 ELM CYCLE SYNCHRONIZATION

•

### 4.3 EPED MODEL PREDICTIONS

•

### 4.4 $I_p$ SCAN

•

### 4.5 PEDESTAL WIDTH SCALINGS

★



## BIBLIOGRAPHY

---



# 5

## I-MODE PEDESTAL SCALINGS

---

### 5.1 ACCESS AND EXPERIMENTAL SETUP

•

### 5.2 PEDESTAL RESPONSES

#### 5.2.1 *Pedestal Response to Fueling*

#### 5.2.2 *Pedestal Temperature*

#### 5.2.3 *Pressure Pedestal Scalings and Performance*

•

### 5.3 PEDESTAL WIDTHS

•

### 5.4 FLUCTUATION CHARACTERIZATION

★



## BIBLIOGRAPHY

---



# 6

## I-MODE PEDESTAL STABILITY MODELING

---

### 6.1 MHD STABILITY – ELITE

•

### 6.2 KBM AND INFINITE- $n$ MHD STABILITY

•

### 6.3 SAWTOOTH PERTURBATIONS OF PEDESTAL STABILITY

unknown!!!

•

### 6.4 OTHER MODELS

★



## BIBLIOGRAPHY

---



# 7

## CONCLUSIONS

---

•



## BIBLIOGRAPHY

---



# A

## DIAGNOSTICS

---

The dedicated pedestal experiments, both in I-mode and ELMy H-mode, presented here required an extensive suite of diagnostics to characterize pedestal behavior. Broadly, these diagnostics may be broken down into three categories:

### THOMSON SCATTERING

Details the edge Thomson scattering diagnostic, from which the high-resolution profile data used for the bulk of this thesis was gathered.

### FAST DIAGNOSTICS

Details the Electron-Cyclotron Emission (ECE) and  $H_{\alpha}$  line radiation diagnostics used to track sawtooth crashes and ELM events in the plasma edge.

### FLUCTUATION DIAGNOSTICS

Details Gas-Puff Imaging (GPI), Reflectometry, and other diagnostics used to characterize the mid-frequency fluctuations found in I-mode pedestals.

•

#### A.1 THOMSON SCATTERING

Due to the steep gradients in density, temperature, and pressure found in the pedestal, accurate characterization of plasma profiles in this region requires diagnostics capable of very fine spatial resolution. Measurements based on the Thomson scattering [1] of laser light off of electrons in the plasma provides the high-resolution pedestal profiles used in this thesis: Thomson scattering is a near-direct measurement of electron temperature and density, independent of bulk plasma parameters (i.e., it is unaffected by the cutoffs or reflections found in other diagnostics, and produces no significant perturbation to the plasma). Measurement via Thomson scattering produces an effective “snapshot” of the plasma parameters at each measurement point, with spatial resolution limited only by collection optics geometry, and time resolution limited by repetition rate on the lasers. Despite significant technical difficulties – for example, the high-powered lasers and sensitive collection optics needed to capture the weak scattered light and the necessity for careful calibration of density measurements – Thomson scattering diagnostics remain a versatile and powerful tool for plasma pedestal measurement, and provided the bulk of the profile data used in this thesis.

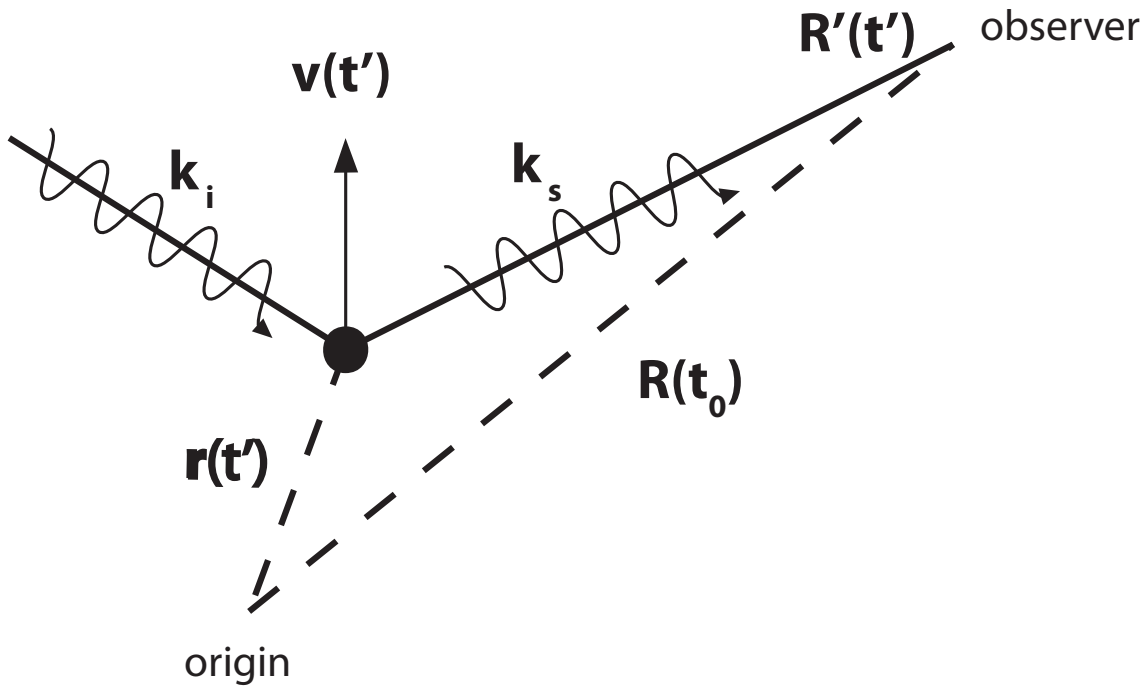


**Figure A.1:** Coordinate system considered for Thomson scattering, with the incident wave of wavenumber  $\vec{k}_i$  incident on a particle at  $\vec{r}(t')$  for retarded time  $t'$ . The scattered wave  $\vec{k}_s$  is drawn to an observer at  $\vec{R}(t')$ .

### A.1.1 Principles of Thomson Scattering

An intuitive picture of the Thomson scattering phenomenon may be obtained by the consideration of a stationary, free electron with an EM wave impinging on it. The particle will be accelerated by the wave (approximately sinusoidally for E-field-dominated acceleration at nonrelativistic speeds), causing it to radiate. Any motion of the electron will cause Doppler shifting in the scattered radiation – motion relative to the incident wave shifts the incident frequency  $\omega_i$ , at which the particle oscillates, while motion relative to an observer shifts the scattered wave. This geometry for general positions of the particle and observer is given in fig. A.1.

The scattered electric field from a generally-accelerated electron moving at  $\beta = \vec{v}/c$  is given from the Lienard-Wiechert potentials [2, §7],

$$\vec{E}_s = \frac{-e}{4\pi\epsilon_0} \left[ \frac{1}{\kappa^3 R c} \hat{s} \times \left( (\hat{s} \times \vec{\beta}) \times \dot{\beta} \right) \right]_{t'} \quad (A.1)$$

$$\kappa = 1 = \frac{\vec{R}' \cdot \vec{v}}{R' c} = 1 - \hat{s} \cdot \vec{\beta}, \quad t' = t - \frac{R'}{c}$$

where  $\hat{s}$  indicates the unit vector along the scattering direction,  $\vec{R} = R\hat{s}$  is the vector to the observer,  $\kappa$  is a relativistic scale factor, and  $t'$  is the relativistic retarded time. The apostrophe indicates a parameter

evaluated at the retarded time, i.e.,  $R' = R(t')$ ; the bracketed term in eq. (A.1) likewise is evaluated at  $t'$ . The scattered power per solid angle is given by

$$\begin{aligned}\frac{dP_s}{d\Omega} &= R^2 \vec{S} \cdot \hat{s} = R^2 \frac{1}{\mu_0} (\vec{E} \times \vec{B}) \cdot \hat{s} \\ &= R^2 \epsilon_0 c (\vec{E}_s \times (\hat{s} \times \vec{E}_s)) \cdot \hat{s} = R^2 c \epsilon_0 |E_s|^2\end{aligned}\quad (\text{A.2})$$

Relativistically, the electron motion (which in turn sets the field determined by eq. (A.1)) is given by

$$\dot{\beta} = \frac{d}{dt} (\gamma m_e \vec{v}) = -e (\vec{E}_i + \vec{v} \times \vec{B}_i) \quad (\text{A.3})$$

thus

$$m_e \gamma \dot{\beta} + \gamma^3 m_e \beta (\vec{\beta} \cdot \dot{\beta}) = -e \left( \frac{\vec{E}_i}{c} + \vec{\beta} \times \vec{B}_i \right) \quad (\text{A.4})$$

Dotting  $\vec{\beta}$  into this and substituting,

$$\dot{\beta} = -\frac{e}{m_e \gamma} \left( \frac{\vec{E}_i}{c} - \frac{\vec{\beta} \cdot \vec{E}_i}{c} \vec{\beta} + \vec{\beta} \times \vec{B}_i \right) \quad (\text{A.5})$$

The general relativistic solution to eqs. (A.1) and (A.2) with the above is rather intractible, although full relativistic treatments have been undertaken [3, 4, 5, 6]. However, the radiated field may be simplified substantially in the nonrelativistic limit – in the limit of  $\beta \ll 1$ , the acceleration is simply

$$\dot{\beta} = -\frac{e}{m_e c} \vec{E}_i \quad (\text{A.6})$$

and the scattered field is

$$\vec{E}_s = \frac{e^2}{4\pi\epsilon_0 m_e c^2} \left[ \left[ \frac{1}{R} \hat{s} \times (\hat{s} \times \vec{E}_i) \right] \right]_{t'}, \quad (\text{A.7})$$

Recalling the classical electron radius,

$$r_e = \frac{e^2}{4\pi\epsilon_0 m_e c^2} \quad (\text{A.8})$$

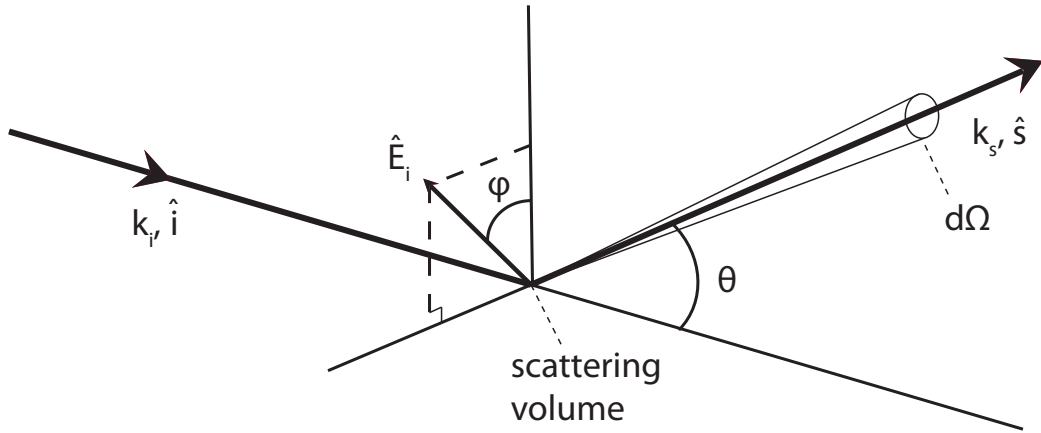


**Figure A.2:** Definitions of the angular dependences in the Thomson scattering geometry: namely, the angle  $\theta$  between the incident wave direction  $\hat{i}$  and scattering direction  $\hat{s}$ , and the polarization angle  $\phi$  of the incident electric field  $\hat{E}_i$  with respect to the projection of  $\hat{s}$  into the polarization plane.

the radiated power is given by

$$\frac{dP_s}{d\Omega} = r_e^2 c \epsilon_0 E_{i0}^2 \llbracket \hat{s} \times (\hat{s} \times \hat{E}_i) \rrbracket^2 \cos^2(\vec{k}_i \cdot \vec{r}' - \omega_i t') \quad (\text{A.9})$$

separating the magnitude, direction, and phase (evaluated at  $t'$ ) of the incident field.

We may first consider the scattering direction dependence,

$$\llbracket \hat{s} \times (\hat{s} \times \hat{E}_i) \rrbracket_{t'}^2 \quad (\text{A.10})$$

Defining the angular geometry as in fig. A.2 for the scattering angle  $\theta$  between the incident wave direction  $\hat{i}$  and scattering direction  $\hat{s}$ , and the polarization angle  $\phi$  (defined between  $\hat{E}_i$  and the projection of  $\hat{s}$  into the polarization plane), this reduces to (cf. [1, §1.7])

$$\llbracket \hat{s} \times (\hat{s} \times \hat{E}_i) \rrbracket^2 = 1 - \sin^2 \theta \cos^2 \phi \quad (\text{A.11})$$

Since the incident power flux is given by

$$S_i = c \epsilon_0 E_{i0}^2 \cos^2(\vec{k}_i \cdot \vec{r}' - \omega_i t') \quad (\text{A.12})$$

We may separate the incident flux and scattering by

$$\frac{dP}{d\Omega} = S_i \frac{d\sigma_t}{d\Omega} \Rightarrow \frac{d\sigma_t}{d\Omega} = r_e^2 [1 - \sin^2 \theta \cos^2 \phi] \quad (\text{A.13})$$

defining a scattering cross-section  $\sigma_t$ . Integrating over  $d\Omega$ ,

$$\sigma_t = \frac{8\pi}{3} r_e^2 = 6.65 \times 10^{-29} \text{ m}^2 \quad (\text{A.14})$$

The extremely small cross-section for Thomson scattering necessitates high-powered lasers and sensitive collection optics – for example, the fraction of photons scattered from a segment along the laser beam path of length  $L$  with electron density  $n_e$  is given simply by  $L n_e \sigma_t$ . For  $L = 1 \text{ mm}$  and  $n_e = 1 \times 10^{20} \text{ m}^{-3}$ , Thomson scattering faces an attenuation factor on the order of  $\sim 10^{-11}$  to the incident photon count from the laser.

The phase of the scattered wave is determined by a retarded-time evaluation of the incident phase,  $\vec{k}_i \cdot \vec{r}(t') - \omega_i t'$ . Substituting  $\vec{r}(t') = \vec{r}_0 + \vec{v}t'$ , and assuming  $R(t') \approx R(t_0)$  (which holds for observers far from the scattering volume,  $R \gg r$ ) we may rewrite the retarded time as

$$t' = \frac{1}{1 - \hat{s} \cdot \vec{\beta}} \left( 1 - \frac{R}{c} + \frac{\hat{s} \cdot \vec{r}_0}{c} \right) \quad (\text{A.15})$$

Substituting, the phase argument becomes

$$k_i \frac{1 - \hat{i} \cdot \vec{\beta}}{1 - \hat{s} \cdot \vec{\beta}} R - \omega_i \frac{1 - \hat{i} \cdot \vec{\beta}}{1 - \hat{s} \cdot \vec{\beta}} t - k_i \frac{1 - \hat{i} \cdot \vec{\beta}}{1 - \hat{s} \cdot \vec{\beta}} \hat{s} \cdot \vec{r}_0 + \vec{k}_i \cdot \vec{r}_0 \quad (\text{A.16})$$

where  $\hat{i}$  is the incident wave propagation direction. We have naturally arrived at the Doppler-shifted frequency,

$$\begin{aligned} \omega_s &= \frac{1 - \hat{i} \cdot \vec{\beta}}{1 - \hat{s} \cdot \vec{\beta}} \omega_i \\ \vec{k}_s &= k_i \frac{1 - \hat{i} \cdot \vec{\beta}}{1 - \hat{s} \cdot \vec{\beta}} \hat{s} = \frac{\omega_s}{c} \hat{s} \end{aligned} \quad (\text{A.17})$$

so the phase is

$$\vec{k}_i \cdot \vec{r}' - \omega_i t' = k_s R - \omega_s t + (\vec{k}_s - \vec{k}_i) \cdot \vec{r}_0 \quad (\text{A.18})$$

Alternately, we may define

$$\begin{aligned} \vec{k} &= \vec{k}_s - \vec{k}_i \\ \omega &= \omega_s - \omega_i = \vec{k} \cdot \vec{v} \end{aligned} \quad (\text{A.19})$$

We may establish the frequency spectrum of the scattered radiation by taking the Fourier transform of the scattered field,

$$\vec{E}_s(\omega_s) = \int \vec{E}_s(t) e^{i\omega_s t} dt \quad (\text{A.20})$$

At retarded time,  $dt = \kappa' dt'$ , and

$$\vec{E}_s(\omega_s) = \frac{r_e}{R'} \int \kappa' \Pi \cdot \vec{E}_i(\vec{r}', t') e^{-\omega_s (t' + \frac{R'}{c} - \frac{\hat{s} \cdot \vec{r}'}{c})} dt' \quad (\text{A.21})$$

Here, for generality we use the polarization tensor  $\Pi$ , which includes relativistic effects – in the nonrelativistic limit  $\Pi = \hat{s}\hat{s} - \mathbf{I}$  such that  $\Pi \cdot \vec{E}_i = \hat{s} \times (\hat{s} \times \vec{E}_i)$ . Using  $\vec{E}_i(\vec{r}, t) = \vec{E}_{i0} \exp(i(\vec{k}_i \cdot \vec{r} - \omega_i t))$  and eq. (A.19),

$$\vec{E}_s(\omega_s) = \frac{r_e}{R'} e^{ik_s R'} \int \kappa' (\Pi \cdot \hat{E}_i) E_{i0} e^{i(\omega t' - \vec{k} \cdot \vec{r}')} dt' \quad (\text{A.22})$$

Integrating and substituting  $\omega_s = 2\pi\nu_s$ ,

$$\vec{E}_s(\nu_s) = \frac{r_e}{R'} e^{ik_s R} 2\pi \kappa (\Pi \cdot \vec{E}_{i0}) \delta(\vec{k} \cdot \vec{v} - \omega) \quad (\text{A.23})$$

We may thus construct the scattered power per solid angle per unit frequency

$$\frac{d^2 P}{d\Omega d\nu_s} = r_e^2 |\Pi \cdot \hat{E}_i|^2 (c \epsilon_0 E_{i0}^2) \delta \left( \nu_s - \frac{1 - \hat{i} \cdot \vec{\beta}}{1 - \hat{s} \cdot \vec{\beta}} \nu_i \right) \quad (\text{A.24})$$

So we have established the scattered power spectrum in solid angle and frequency of a single electron as a function of scattering direction (encoded in  $\Pi \cdot \hat{E}_i$ ) and incident laser energy (in the incident Poynting flux  $\langle S_i \rangle = c \epsilon_0 E_{i0}^2$ ). The scattered spectrum locked to a single frequency by the Dirac delta function, forcing the scattered spectrum to radiate strictly at the Doppler-shifted frequency set by the electron motion.

To consider the spectrum from a population of electrons, we must consider the interactions between nearby electrons. On length scales comparable to the electron Debye length  $\lambda_{De}$  (eq. (1.1)), electrons in the plasma screen out incident electric fields – this organized motion leads to interference in the scattered radiation, referred to as *collective*

or *coherent scattering*. The full solution for the scattered spectrum (see [1, §3]) may be expanded in a series in the factor

$$\alpha = \frac{1}{k\lambda_{De}} \quad (\text{A.25})$$

Coherent effects are negligible in the limit of  $\alpha \ll 1$ , at which the scattering is said to be *incoherent* or *noncollective* – the radiation from a population of electrons is simply the sum of each individual contribution. For the effective scattering wavevector,  $\vec{k} = \vec{k}_s - \vec{k}_i$  (eq. (A.19)),

$$\begin{aligned} |\vec{k}| &= \sqrt{k_s^2 + k_i^2 - 2k_s k_i \cos \theta} \\ &\approx \sqrt{2} k_i \sqrt{1 - \cos \theta} = \sqrt{2} k_i \sqrt{2 \sin^2 \left( \frac{\theta}{2} \right)} \end{aligned} \quad (\text{A.26})$$

assuming  $k_s \approx k_i$ . Thus the noncollective requirement reduces to

$$\frac{1}{2k_i \sin(\theta/2)\lambda_{De}} \ll 1 \Rightarrow \frac{\lambda_i}{\lambda_{De}} \ll 4\pi \sin \left( \frac{\theta}{2} \right) \quad (\text{A.27})$$

This condition is readily satisfied at near-perpendicular scattering ( $\theta \approx 90^\circ$ , where the scattering amplitude is maximized) and with laser wavelengths much smaller than the Debye length ( $\lambda_{De} \sim 10 - 100 \mu\text{m}$  at tokamak conditions, compared to the  $\lambda_i \sim 1 \mu\text{m}$  IR lasers commonly used for Thomson scattering photon sources).

Thus, the incoherent scattered spectrum is simply the sum of contributions from each electron in the scattering volume – the spectrum from a population described by the distribution function  $f_e(\vec{r}, \vec{v})$  is

$$\frac{d^2P}{d\Omega dv_s} = 2\pi r_e^2 \int_V \langle S_i \rangle \int |\Pi \cdot \hat{E}_i|^2 f_e(\vec{r}, \vec{v}) \kappa^2 \delta(\vec{k} \cdot \vec{v} - \omega) d^3v d^3r \quad (\text{A.28})$$

For small scattering volumes, the electron distribution function is approximately uniform in space. In the nonrelativistic limit,  $\Pi \cdot \hat{E}_i$  is independent of velocity, thus the spatial contribution may be separated out:

$$\int_V \langle S_i \rangle |\Pi \cdot \hat{E}_i|^2 d^3r \quad (\text{A.29})$$

encoding the incident photon flux (from the Poynting vector of the laser) and the scattering direction dependence. The velocity integral (noting  $\kappa \approx 1$  in the nonrelativistic case) is

$$\int f(\vec{v}) \delta(\vec{k} \cdot \vec{v} - \omega) d^3 \vec{v} \quad (\text{A.30})$$

Splitting the velocity into components parallel and perpendicular to  $\vec{k}$ ,  $\vec{v}_\perp$ ,  $\vec{v}_k$ , this is

$$\int f(\vec{v}_\perp, \vec{v}_k) \delta(kv_k - \omega) d^2 \vec{v}_\perp dv_k = \int f_k(v_k) \delta(kv_k - \omega) dv_k \quad (\text{A.31})$$

utilizing the normalization required for  $f(\vec{v})$  to solve the integrals over  $\vec{v}_\perp$ . For a Maxwellian (eq. (1.5)) the distribution along the effective wavevector  $\vec{k}$  is

$$f_k(v_k) = n_e \frac{1}{v_t \sqrt{\pi}} e^{-v_k^2/v_t^2} \quad (\text{A.32})$$

thus the above is solvable,

$$\int f_k(v_k) \delta(kv_k - \omega) dv_k = \frac{1}{k} f_k \left( \frac{\omega}{k} \right) \quad (\text{A.33})$$

Substituting into eq. (A.28),

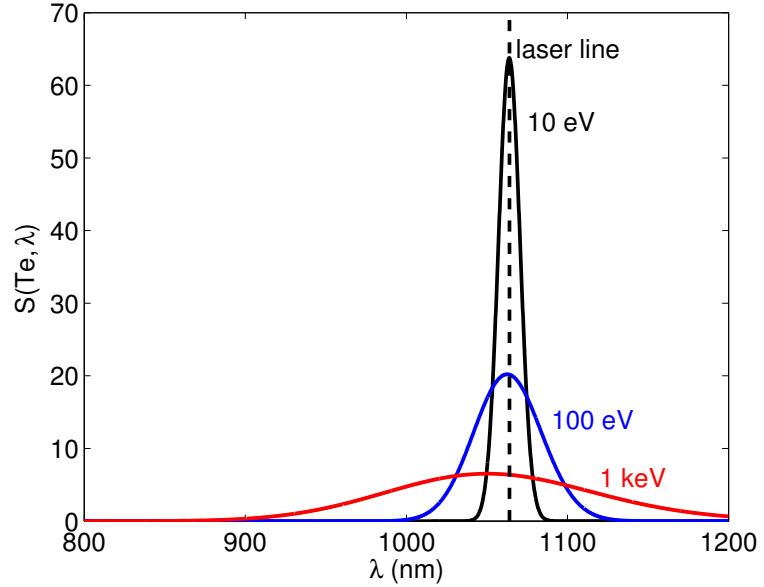
$$\begin{aligned} \frac{d^2 P}{d\Omega dv_s} &= 2\pi r_e^2 \left[ \int_V \langle S_i \rangle |\hat{s} \times (\hat{s} \times \hat{E}_i)|^2 d^3 \vec{r} \right] \times \\ &\quad \frac{1}{\sqrt{\pi k}} \frac{n_e}{v_t} \exp \left( -\frac{\omega^2}{k^2 v_t^2} \right) \end{aligned} \quad (\text{A.34})$$

Substituting  $k \approx 2k_i \sin(\theta/2) = (4\pi/\lambda_i) \sin(\theta/2)$ , the exponent is

$$-\frac{(\omega_s - \omega_i)^2}{4 \frac{4\pi^2}{\lambda_i^2} \sin^2(\theta/2) v_t^2} \approx -\frac{c^2 (\lambda_s - \lambda_i)^2}{4 \lambda_i^2 v_t^2 \sin^2(\theta/2)} \quad (\text{A.35})$$

Converting from a frequency to a wavelength spectrum, and assuming the scattering volume to be sufficiently small that the scattering angle and incident Poynting flux are uniform (thus  $\int \langle S_i \rangle d^3 \vec{r} =$

**Figure A.3:** Spectral functions normalized to density and laser power, evaluated at  $\theta = \phi = \pi/2$ . The spectrum spreads farther from the laser line at higher temperature, as well as blue-shifting due to relativistic effects.



$\langle S_i \rangle AL = P_i L$  for laser cross-section  $A$ , scattering volume  $L$ , and laser power  $P_i$ ) the nonrelativistic scattering spectrum is

$$\frac{d^2P}{d\Omega d\lambda_s} = P_i r_e^2 n_e L |\hat{s} \times (\hat{s} \times \hat{E}_i)|^2 S(T_e, \theta, \lambda_s)$$

$$S(T_e, \theta, \lambda_s) = \frac{1}{2\sqrt{\pi} \sin(\theta/2)} \frac{c}{\lambda_i v_t} \exp\left(-\frac{c^2(\lambda_s - \lambda_i)^2}{4v_t^2 \lambda_i^2 \sin^2(\theta/2)}\right) \quad (\text{A.36})$$

This expression is a Maxwellian centered at  $\lambda = \lambda_i$  with a spread determined by the electron temperature  $T_e$  (manifesting in the thermal velocity  $v_t$ ) and the scattering angle  $\theta$ . Recalling the angle  $\phi$  defined between the incident polarization  $\hat{E}_i$  and the scattering direction  $\hat{s}$ ,  $|\hat{s} \times (\hat{s} \times \hat{E}_i)|^2 = \sin^2 \phi$  is maximized for scattering perpendicular to the incident laser polarization.

*ref to figure*

This analysis breaks down for relativistic electron populations. However, relativistic effects (see [1, §9]) may be expressed as a polynomial correction to eq. (A.36),

$$S_{\text{rel}}(T_e, \theta, \lambda_s) = S(T_e, \theta, \lambda_s) \left[ 1 - \frac{3.5(\lambda_s - \lambda_i)}{\lambda_i} + \frac{c^2(\lambda_s - \lambda_i)^3}{4v_t^2 \lambda_i^2 \sin^2(\theta/2)} \right] \quad (\text{A.37})$$

The relativistic correction breaks the symmetry of the Maxwellian spectrum, introducing a net blue shift to the spectrum. Physically, this is due to “relativistic headlighting,” in which the radiation from an accelerating relativistic particle is biased forward of its motion – The radiated power is stronger from particles moving toward the observer

(thus with a blue Doppler shift to their emissions). The spectral form factor  $S(T_e, \theta, \lambda_s)$  is shown in figure fig. A.3, illustrating the width dependence of the spectrum on the electron temperature and the blue shifting evident in the spectrum even at relatively low plasma temperatures.

Examination of eqs. (A.36) and (A.37) readily illustrates the method for extracting  $n_e$  and  $T_e$  measurements from the Thomson scattering spectrum – the spread of the spectrum of scattered radiation is directly tied to the electron temperature, while the integrated amplitude gives electron density (as the total scattered power is linearly proportional to  $n_e$ ). Assumptions regarding the Maxwellian distribution of the electrons allows accurate measurement of the electron profile with relatively simple hardware, detailed in the next section.

#### A.1.2 Edge Thomson Scattering on C-Mod

### A.2 FAST DIAGNOSTICS

### A.3 FLUCTUATION DIAGNOSTICS

## BIBLIOGRAPHY

---

- [1] J. Sheffield. *Plasma scattering of electromagnetic radiation*. Academic Press, 1975.
- [2] I.H. Hutchinson. *Principles of Plasma Diagnostics*. Cambridge University Press, 2005.
- [3] J. Sheffield. The incoherent scattering of radiation from a high temperature plasma. *Plasma Physics*, 14(8):783, 1972.
- [4] T. Matoba, T. Itagaki, T. Yamauchi, and A. Funahashi. Analytical approximations in the theory of relativistic thomson scattering for high temperature fusion plasma. *Japanese Journal of Applied Physics*, 18(6):1127–1133, 1978.
- [5] A. C. Selden. Simple analytic form of the relativistic thomson scattering spectrum. *Physics Letters A*, 79(5-6):405 – 406, 1980.
- [6] O. Naito, H. Yoshida, and T. Matoba. Analytic formula for fully relativistic thomson scattering spectrum. *Physics of Fluids B: Plasma Physics*, 5(11):4256–4258, 1993.



# B

## HIGH-RESOLUTION PEDESTAL DATABASE

For the work presented in this thesis, a subset of recent I-mode experiments on Alcator C-mod was prepared with high-resolution pedestal data. These data are stored in an SQL database under the C-Mod “log-book” system. Use of an SQL table enables efficient cross-platform access to pedestal data in a format ideal for data mining, and allows for easy extensibility of stored parameters for additional experiments. The database stores windows of data in which plasma parameters (e.g., temperature, stored energy, density, heating power) are steady – usable phases last at least  $\sim 100$  ms ( $\sim 10$  Thomson scattering frames), over which frames of TS pedestal data are averaged. For each phase, the SQL database stores a variety of physics and engineering parameters, and scalar fitting parameters for the pedestal. For direct comparison, the table also stores analogous data from L- and H-mode phases.

*point to mtanh  
fitting function*

**Table B.1:** SQL database parameters used as keys – (SHOT, TA, TB) is sufficient to uniquely identify entries in the database.

<i>column</i>	<i>data type</i>	<i>units</i>	<i>description</i>
SHOT	long		C-Mod shot number
TA	long	ms	start time of phase
TB	long	ms	end time of phase

★

**Table B.2:** SQL database parameters used as flags for time windows.

<i>column</i>	<i>data type</i>	<i>units</i>	<i>description</i>
MODE	string		type of phase in window, e.g., 'IMODE', 'ELMY', 'EDA', 'LMODE'
ELMS	int		binary flag, = 1 for ELMs in phase
LH	int		binary flag, = 1 for LHCD in phase
WCM	int		binary flag, = 1 for WCM
TREE_PATH	string		fluctuation in phase (I-mode only) path to branch in pedestal-profile MDS tree
TREE_SHOT	long		shot number flagged in pedestal-profile MDS tree, used to differentiate sub-branches of a single shot

**Table B.3:** SQL database parameters for useful measured parameters.

<i>column</i>	<i>data type</i>	<i>units</i>	<i>description</i>
NLo4	float	$\text{m}^{-2}$	line-integrated density from TCI
NLo4_ERR	float	$\text{m}^{-2}$	error in NLo4
NEBAR	float	$\text{m}^{-3}$	line-averaged density from TCI
NEBAR_ERR	float	$\text{m}^{-3}$	error in NEBAR
ECE_To	float	eV	core electron temperature from ECE
ECE_TPED	float	eV	pedestal electron temperature from ECE (channel nearest 95% flux surface)
NEo	float	$\text{m}^{-3}$	core density from TS
NEo_ERR	float	$\text{m}^{-3}$	error in NEo
TEo	float	eV	core temperature from TS
TEo_ERR	float	eV	error in TEo
NUSTAR	float		pedestal collisionality at 95% flux surface
RHOSTAR	float		pedestal normalized gyroradius at 95% flux surface
ZEFF	float		average effective charge
ZEFF_ERR	float		error in ZEFF measurement

**Table B.4:** SQL database parameters for EFIT values.

<i>column</i>		<i>data type</i>	<i>units</i>	<i>description</i>
KAPPA		float		plasma elongation $\kappa$ (see fig. 1.6)
KAPPA_ERR		float		error in KAPPA
DELTA_U		float		plasma upper triangularity (see fig. 1.6)
DELTA_U_ERR		float		error in DELTA_U
DELTA_L		float		plasma lower triangularity (see fig. 1.6)
DELTA_L_ERR		float		error in DELTA_L
IP		float	MA	plasma current
IP_ERR		float	MA	error in IP
DIDT		float	MA s <sup>-1</sup>	change in plasma current $dI_p/dt$
DIDT_ERR		float	MA s <sup>-1</sup>	error in DIDT
BT		float	T	axial toroidal field
BT_ERR		float	T	error in BT
BP		float	T	flux-surface averaged edge poloidal field
BP_ERR		float	T	error in BP
Q <sub>0</sub>		float		axial safety factor $q_0$
Q <sub>0</sub> _ERR		float		error in Q <sub>0</sub>
Q <sub>95</sub>		float		edge safety factor $q_{95}$
Q <sub>95</sub> _ERR		float		error in Q <sub>95</sub>
R		float	cm	major radius
A		float	cm	outboard-midplane minor radius
SSEP		float	?	separatrix separation?
BETAT		float		global toroidal beta, $\langle \beta_t \rangle$
BETAP		float		global poloidal beta, $\langle \beta_p \rangle$
BETAN		float	m T MA <sup>-1</sup>	global normalized beta, $\beta_N = \langle \beta \rangle / (I_p/aB_t)$
TAU_MHD		float	s	MHD energy confinement time, $\tau_E$
TAU_MHD_ERR		float	s	error in TAU_MHD

**Table B.5:** SQL database parameters for heating power, stored energy, and confinement.

<i>column</i>	<i>data type</i>	<i>units</i>	<i>description</i>
PLASMA_W	float	J	plasma stored energy
PLASMA_W_ERR	float	J	error in PLASMA_W
DWDT	float	W	change in stored energy, $dW_{\text{plasma}}/dt$
DWDT_ERR	float	W	error in DWDT
P_ICRF	float	MW	absorbed ICRF heating power
P_ICRF_ERR	float	MW	error in P_ICRF
P_OHM	float	MW	Ohmic heating power
P_OHM_ERR	float	MW	error in P_OHM
P_LH	float	MW	absorbed lower-hybrid heating power
P_LH_ERR	float	MW	error in P_LH
P_RAD	float	MW	radiated power from bolometry
P_RAD_ERR	float	MW	error in P_RAD
P_SOL	float	MW	power through SOL <b>check this!!!</b>
P_SOL_ERR	float	MW	error in P_SOL
P_THRES	float	MW	H-mode threshold power <b>citation?</b>
P_THRES_ERR	float	MW	error in P_THRES
H	float		ITER98y2 H-mode confinement scaling, $H_{98} = \tau_E / \tau_{98y2}$
H_ERR	float		error in H
H89	float		ITER89 L-mode confinement scaling, $H_{89} = \tau_E / \tau_{89}$
H89_ERR	float		error in H89

**Table B.6:** SQL database parameters for high-resolution pedestal profiles.

<i>column</i>	<i>data type</i>	<i>units</i>	<i>description</i>
NEPED_H	float	$\text{m}^{-3}$	density pedestal height
NEPED_H_ERR	float	$\text{m}^{-3}$	error in NEPED_H
NEPED_B	float	$\text{m}^{-3}$	density pedestal baseline
NEPED_B_ERR	float	$\text{m}^{-3}$	error in NEPED_B
NEPED_D	float		density pedestal half-width
NEPED_D_ERR	float		error in NEPED_D
NEPED_Ro	float		density pedestal midpoint
NEPED_Ro_ERR	float		error in NEPED_Ro
NEPED_ALPHA	float		density pedestal inboard-slope parameter
NEPED_ALPHA_ERR	float		error in NEPED_ALPHA
NEPED_GRAD	float	$\text{m}^{-3}$	peak density pedestal gradient (pedestal midpoint)
NEPED_GRAD_ERR	float	$\text{m}^{-3}$	error in NEPED_GRAD
NEPED_LGRAD	float		peak density pedestal gradient scale length
NEPED_LGRAD_ERR	float		error in NEPED_LGRAD
NEPED_95	float	$\text{m}^{-3}$	density at 95% flux surface
NEPED_95_ERR	float	$\text{m}^{-3}$	error in NEPED_95
TEPED_H	float	eV	temperature pedestal height
TEPED_H_ERR	float	eV	error in TEPED_H
TEPED_B	float	eV	temperature pedestal baseline
TEPED_B_ERR	float	eV	error in TEPED_B
TEPED_D	float		temperature pedestal half-width
TEPED_D_ERR	float		error in TEPED_D
TEPED_Ro	float		temperature pedestal midpoint
TEPED_Ro_ERR	float		error in TEPED_Ro
TEPED_ALPHA	float		temperature pedestal inboard-slope parameter
TEPED_ALPHA_ERR	float		error in TEPED_ALPHA
TEPED_GRAD	float	eV	peak temperature pedestal gradient (pedestal midpoint)
TEPED_GRAD_ERR	float	eV	error in TEPED_GRAD
TEPED_LGRAD	float		peak temperature pedestal gradient scale length
TEPED_LGRAD_ERR	float		error in TEPED_LGRAD
TEPED_95	float	eV	temperature at 95% flux surface
TEPED_95_ERR	float	eV	error in TEPED_95
PEPED_H	float	$/ \text{m}^3 \text{ eV}$	pressure pedestal height
PEPED_H_ERR	float	$/ \text{m}^3 \text{ eV}$	error in PEPED_H
PEPED_B	float	$/ \text{m}^3 \text{ eV}$	pressure pedestal baseline
PEPED_B_ERR	float	$/ \text{m}^3 \text{ eV}$	error in PEPED_B

**Table B.7:** SQL database parameters for WCM fluctuation measurements.

<i>column</i>	<i>data type</i>	<i>units</i>	<i>description</i>
WCM_AMP	float		normalized peak amplitude of WCM from reflectometry
WCM_FREQ	float	kHz	centroid frequency of WCM from reflectometry
WCM_WID	float	kHz	spectral width of WCM determined by $\pm\sigma$ of Gaussian fit on reflectometry
WCM_AMP_PCI	float		normalized peak amplitude of WCM from PCI
WCM_FREQ_PCI	float	kHz	centroid frequency of WCM from PCI
WCM_WID_PCI	float	kHz	spectral width of WCM determined by $\pm\sigma$ of Gaussian fit on PCI

## COLOPHON

This document was typeset using `classicthesis` developed by André Miede (although aspects were changed to comply with the MIT thesis standards and the author's personal preferences). The style was inspired by Robert Bringhurst's seminal book on typography "*The Elements of Typographic Style*". `classicthesis` is available for both L<sup>A</sup>T<sub>E</sub>X and L<sup>A</sup>T<sub>E</sub>X:

<http://code.google.com/p/classicthesis/>

Hermann Zapf's *Palatino* and *Euler* type faces (Type 1 PostScript fonts *URW Palladio L* and *FPL*) are used. The "typewriter" text is typeset in *FPL*, originally developed by Bitstream, Inc. as "Bitstream Vera". (Type 1 PostScript fonts were made available by Malte Rosenau and Ulrich Dirr.)